

---

**Distribution Agreement**

In presenting this thesis or dissertation as a partial fulfillment of the requirements for an advanced degree from Emory University, I hereby grant to Emory University and its agents the non-exclusive license to archive, make accessible, and display my thesis or dissertation in whole or in part in all forms of media, now or hereafter known, including display on the world wide web. I understand that I may select some access restrictions as part of the online submission of this thesis or dissertation. I retain all ownership rights to the copyright of the thesis or dissertation. I also retain the right to use in future works (such as articles or books) all or part of this thesis or dissertation.

Signature:

Jin Liu

05/12/2012

\_\_\_\_\_  
[Student's name typed]

\_\_\_\_\_  
Date

---

Use of Receptor-Based Drug Design and Applications in the Study of  
finding antagonists for MD-2/TLR4, GLP and CXCR4

By

Jin Liu  
Doctor of Philosophy  
Chemistry

---

Dennis C. Liotta, Ph.D.  
Advisor

---

James P. Snyder, Ph.D.  
Advisor

---

James T. Kindt, Ph.D.  
Committee Member

---

Vince Conticello, Ph.D.  
Committee Member  
Accepted:

---

Lisa A. Tedesco, Ph.D.  
Dean of the James T. Laney School of Graduate Studies

---

Date

Use of Receptor-Based Drug Design and Applications in the Study of  
finding antagonists for MD-2/TLR4, GLP and CXCR4

By

Jin Liu  
B.S. University of Science and Technology of China

Advisor:  
Dennis C. Liotta, Ph.D.  
James P. Snyder, Ph.D.

An abstract of  
A dissertation submitted to the Faculty of the  
James T. Laney School of Graduate Studies of Emory University  
In partial fulfillment of the requirements for the degree of  
Doctor of Philosophy  
in Chemistry  
2012

## Abstract

### Use of Receptor-Based Drug Design and Applications in the Study of finding antagonists for MD-2/TLR4, GLP and CXCR4

By  
Jin Liu

Paclitaxel (PTX) mimics the action of lipopolysaccharide (LPS) in mice but not in human immune system. Recent experiments show that activation of TLR4 by PTX requires the mouse MD-2 protein, and is independent of TLR4 species, indicating that the mouse MD-2/PTX interaction is a key to TLR4 activation. To define the structural differences for MD-2/TLR4 activation, the electrostatic potential and lipophilic surfaces of human and mouse MD-2 have been assessed. The computational docking of PTX to each species supports the hypothesis that PTX, as an antagonist in human MD-2, stabilized loop 123-130, especially the Phe126, to prevent TLR4/MD-2 dimerization.

Lipopolysaccharide (LPS) signals through a membrane bound-complex of the lipid binding protein MD-2 and the receptor TLR4. When LPS binds MD-2, the complex activates the key transcriptional regulator NF- $\kappa$ B, resulting in the production of inflammatory cytokines. TLR4 dimerization is an essential step in signal transduction. In this study, we identified the human and mouse TLR4/MD-2 dimerization model by computation – Rosetta Protein-Protein docking. The Meningococcal LOS binding modes in human TLR4/MD-2 dimer were also predicted. KDO moiety is crucial for meningococcal LOS bioactivity. PEA group can be added at 1-PO4 or 4-PO4 site to make more tightly binding.

The Gilman reagent can be used for selective creation of carbon-carbon bonds in organic chemistry. We performed density functional calculations to propose a reasonable mechanism for the reaction between  $\text{Me}_2\text{CuLi}\cdot\text{LiX}$  ( $\text{X}=\text{I}, \text{SCH}_3, \text{CN}$ ) and  $\text{CH}_3\text{I}$ . The tetracoordinate, square-planar intermediate proves to be an intermediate species in the calculation. Based on our calculations, the reaction goes through an asymmetric, non-planar transition state to reach the long proposed “copper (III) intermediate”. Then the intermediate overcomes a fairly low barrier to create ethane. The schematic potential energy surface for this reaction illustrates the mechanism for new carbon-carbon bond formation.

Histone lysine methylation plays a key epigenetic role in the regulation of chromatin and gene expression. BIX-01294 (a diazepin-quinazolin-amine derivative) inhibits activities of G9a and G9a-like protein (GLP) lysine methyltransferase. Efforts to improve the potency of BIX-01294 employed the X-ray structure of the GLP/BIX-01294 complex as a template for structure-based design. After the molecular modeling to guide the design, synthesis, and validation of new BIX derivatives, we found that adding a lysine mimic proved to be 5-10 fold more potent than the original compound.

G-protein coupled receptor (GPCR) CXCR4 and the chemokine stromal cell-derived factor-1 (SDF-1/CXCL12) play a crucial role in physiological processes. The interaction of SDF-1 with CXCR4 has implications in cancer metastasis. Several benzenesulfonamide analogs were designed and synthesized to find anti-CXCR4 agents to disrupt of the interaction of SDF-1 with CXCR4. The docking scores of these analogs correlated with the effective concentration of these compounds blocking TN14003 binding on CXCR4.

Use of Receptor-Based Drug Design and Applications in the Study of  
finding antagonists for MD-2/TLR4, GLP and CXCR4

By

Jin Liu  
B.S. University of Science and Technology of China

Advisor:  
Dennis C. Liotta, Ph.D.  
James P. Snyder, Ph.D.

A dissertation submitted to the Faculty of the  
James T. Laney School of Graduate Studies of Emory University  
In partial fulfillment of the requirements for the degree of  
Doctor of Philosophy  
in Chemistry  
2012

**Acknowledgements:**

This thesis is the result of not only my efforts but also those of others who have supported me in different ways all along my Ph.D. program.

I would like to gratefully and sincerely thank Drs. James P Snyder and Dennis C Liotta for their guidance, understanding, patience, and most importantly, their friendship during my graduate studies at Emory University. Their mentorship was paramount in providing a well rounded experience consistent my long-term career goals. For everything you've done for me, Drs. Snyder and Liotta, I thank you.

I would also like to thank my Ph.D. committee members Drs. Conticello and Kindt for their valuable discussions and encouragement.

Additionally, I am very grateful for the friendship of all of the members of Liotta/Snyder research group, especially Dr. Ana Alcaraz, Andrew Prussia, Pahk Thepchatri, Pieter Burger, Haipeng Hu and Mi-Sun Kim who preceded me and gave me so much mentoring. I have enjoyed working with all of you.

## Table of Contents

List of Figures .....	X
List of Tables .....	XII
Chapter 1: Introduction.....	1
1.1 Introduction to drug design.....	1
1.2 Outline for subsequent chapters.....	4
Chapter 2: Paclitaxel binding to Human and Mouse MD-2.....	6
2.1 Introduction.....	6
2.2 Computational Methods.....	11
2.2.1 Homology Modeling.....	11
2.2.2 Computational Ligand-Protein Docking.....	11
2.2.3 Molecular Volumes.....	12
2.3 Results and Discussion.....	13
2.3.1 MD-2 models and Glide Docking.....	13
2.3.2 Induced Fit Docking of PTX into MD-2.....	19
2.3.3 Discussion.....	23
Chapter 3: TLR4/MD-2 dimerization Model.....	27
3.1 Introduction.....	27
3.2 Computational Methods.....	29
3.2.1 Homology Modeling.....	29
3.2.2 Protein-Protein Docking.....	29
3.3 Results and Discussion.....	30
Chapter 4: Lipopolysaccharide (LPS) binding to TLR4/MD-2 dimer.....	36
4.1 Introduction.....	36
4.2 Computational Methods.....	38
4.3 Results and Discussion.....	38
4.3.1 KDO group effect.....	38
4.3.2 PEA group adding to LPS.....	43
Chapter 5: Density Functional Calculation of Cross-Coupling Reaction between series of Gilman Cuprates and CH <sub>3</sub> I.....	47
5.1 Introduction.....	47
5.2 Results and Discussion.....	48
Chapter 6: Structure-based design and synthesis of inhibitors of histone lysine methyltransferase (H3K9me <sub>2</sub> ).....	53
6.1 Introduction.....	53
6.2 Structure-based Modeling of GLP Ligands.....	56
6.2.1 Computational Methods.....	56
6.2.2 Structure-based Prediction of BIX-Analog Binding Poses.....	57
6.3 Conclusion.....	66

---

Chapter 7: Benzenesulfonamides as a New Class of Chemokine Receptor Type 4	
Inhibitors.....	67
7.1 Introduction.....	67
7.2 Results and Discussion.....	69
7.2.1 Structure-Activity Relationship (SAR) Study.....	69
7.2.2 Computational Protein-Ligand Docking.....	70
7.2.3 Mapping of the CXCR4 Antagonists Binding and SDF-1 N-terminus	
Binding.....	70
7.2.4 Prediction of Benzene sulfonamide derivatives Binding Poses.....	72
Reference.....	81

## List of Figures

<b>Figure 1.1</b> Schematic process of structure-based drug design.....	4
<b>Figure 2.1</b> Topological structure of Paclitaxel (top) and 3-D conformation of PTX as observed in $\beta$ -tubulin (bottom).....	8
<b>Figure 2.2</b> hMD-2 crystal structure (left) and mMD-2 crystal structure (right).....	9
<b>Figure 2.3</b> Lipid molecules in hMD-2 bind differently to the cavity mouth.....	15
<b>Figure 2.4</b> Electrostatic potential energy surfaces of MD-2 and MD-2•TLR4 models..	18
<b>Figure 2.5</b> Lipophilic and hydrophobic surfaces of the MD-2 models.....	19
<b>Figure 2.6</b> MD-2•PTX docking poses.....	21
<b>Figure 2.7</b> Detailed view of the top PTX docking pose in human MD-2.....	22
<b>Figure 2.8</b> Comparison between mMD-2 top docking pose and mMD-2 crystal structure .....	22
<b>Figure 3.1</b> Three models of the TLR4-MD-2 dimer are shown.....	31
<b>Figure 3.2</b> The mouse TLR4-MD-2 homodimer (left) and Detailed view of the interface between MD-2 and TLR4 (right).....	33
<b>Figure 3.3</b> The detailed view of the interface between human MD-2 and TLR4 (left); The comparison between the best dimer model of human and mouse (right).....	34
<b>Figure 4.1</b> 2D structure of E. coli lipid A (left) and Neisseria meningitidis lipid A (right) .....	37
<b>Figure 4.2</b> The best docking pose of Meningococcal LPS without KDO.....	39
<b>Figure 4.3</b> The best docking pose of Meningococcal LPS with KDO (left) and the receptor is shown in surface (right).....	40
<b>Figure 4.4</b> Comparison of E.coli LPS and Eritoran after superimposition of MD-2 (left); Comparison of E.coli LPS and lipid IVa.....	42
<b>Figure 4.5</b> Comparison of LPS with KDO and LPS without KDO after superimposition of MD-2.....	43
<b>Figure 4.6</b> 2D structure of Meningococcal 1-PO4-PEA LPS (left) and the docking pose of Meningococcal 1-PO4-PEA LPS.....	44
<b>Figure 4.7</b> The docking pose of Meningococcal 4-PO4-PEA LPS.....	45
<b>Figure 4.8</b> The docking pose of Meningococcal LPS with two PEA groups at each PO4 site.....	46
<b>Figure 5.1</b> The first transition state of cross coupling reaction.....	50
<b>Figure 5.2</b> The intermediate of the cross coupling reaction.....	50
<b>Figure 5.3</b> The schematic potential energy surface for the cross-coupling reaction.....	51
<b>Figure 6.1</b> BIX-01294 centers for structural modification (left); X-ray and Glide docking poses of the ligand in the GLP binding site (right).....	56
<b>Figure 6.2</b> (a)Site A region in BIX-01294 can be populated by different groups; (b) Best docking pose for the N,N-dimethyl-aminopropyl chain in the site A region superimposed with the X-ray structure of BIX-01294.(c) Substituents at site A and best-pose MM-GBSA scores.....	59

---

<b>Figure 6.3</b> (a) BIX analog in which the benzyl moiety has been eliminated; (b) Best docking pose of the benzyl-depleted analog (cyan) superimposed with BIX-01294 in the GLP protein.....	60
<b>Figure 6.4</b> C7-OMe substitution can branch into two channels.....	63
<b>Figure 6.5</b> The protonated dimethylamine coupled to C7-OMe by an n = 6 carbon chain (left) and in its best docking pose within the GLP protein (right).....	63
<b>Figure 6.6</b> The 2D structure of 21a (left) and its Glide-determined docking pose in GLP (right).....	64
<b>Figure 6.7</b> An extended hydrophobic substituent coupled to C7-OMe (left) in its best docking pose within the GLP protein (right).....	64
<b>Figure 6.8</b> 2D structure of BIX-Cn (n=0-7) and their MM-GBSA scores.....	65
<b>Figure 6.9</b> 2D structure of BIX-CnNH <sub>3</sub> <sup>+</sup> (n=1-6) and their MM-GBSA scores.....	65
<b>Figure 7.1</b> 2D structure of WZ119.....	68
<b>Figure 7.2</b> Two regions (A and B) modified for structure-activity relationship study...69	
<b>Figure 7.3</b> Mapping of the SDF-1 N-terminus, T140, and CVX15 binding site; Superposition of SDF-1, T140 and CVX15 binding sites.....	72
<b>Figure 7.4</b> (a) 2D structure of SRM2001; (b) Best docking pose of SRM2001 in CXCR4; (c) Superposition of all active compound best binding poses in CXCR4.....	75
<b>Figure 7.5</b> (a) 2D structure of SRM2015; (b) Best docking pose of SRM2015 in CXCR4 with CVX15; (c) Superposition of best binding poses of SRM2014, SRM2015, and SRM2020 in CXCR4.....	79

## List of Tables

<b>Table 7.1</b> Effective concentration and unscaled binding free energies for active compounds.....	75
<b>Table 7.2</b> Effective concentration and relative binding free energy for inactive compounds.....	78
<b>Table 7.3</b> Effective concentration, IC50 and relative binding free energy for seven compounds.....	80

## Chapter 1

### Introduction

#### 1.1 Introduction to drug design

Drug design is the innovative process of finding new medicines based on the knowledge of a biological target.[1] Drug design involves the design of small molecules which are shape and charge complementary to the biomolecular target, and they will bind to the target through series types of interactions. Since it is time-consuming to discover a new drug, more and more computer approaches are now being developed to reduce the cost and cycle time for discovering a new drug. There are two major types of drug design: one is ligand-based drug design, and the other is structure-based drug design.

Ligand-based drug design was usually employed when the 3-D structure of a target protein is not available. Drug design can instead be based on using the known ligands of a target protein. Molecular similarity approaches, quantitative structure-activity relationships (QSAR) and pharmacophore models are frequently used methods in the ligand-based drug design process.[2]

Structure-based drug design was always used in case that a specific drug target and its 3D structure are known. With the progressing of molecular biology, X-ray crystallography and NMR techniques, the structures of many drug targets have been determined.[3] If an experimental structure of a target is not available, it may be possible to create a homology model of the target based on the experimental structure of a related protein. With the 3D-structure of the biological target, candidate drugs that are predicted to bind with high affinity and selectivity to the target are designed using various automated computational procedures.

Structure-based drug design is a multi-step process. The first step is to obtain the target protein and identify the active site of the target molecules. Then, a series of compounds from compound database or from synthesis are binding into the active site on the target molecule and corresponding docking scores are obtained based on their steric or non-covalent interactions with the target molecule. The top score compounds are recommended to be investigated in the bioassay. These compounds with good activities in the bioassay can be used as lead compound. In the second step, the lead compound is optimized to increase its potency and selectivity. This step contains an iterative cycle including synthesis of the optimized lead, structure determination of the new target-lead complex, and further optimization of the lead compound. After several cycles of the drug design process, the optimized compounds usually show reliable potency and selectivity.

The target protein is usually obtained from X-ray crystallography and NMR techniques. However, in some cases, an experimental structure of a target is not

available. It is necessary to perform homology modeling of the target based on the experimental structure of a related protein with high sequence identity. Various homology modeling tools are developed, such as Prime,[4] Rosetta,[5] and Modeller[6]. No matter which homology modeling tool is adopted, a reasonable sequence alignment is necessary and will affect the final quality of the homology model. After the 3D structure of the target is determined, the next step is finding the active site on the target. In many cases, the resolved crystal structures have already contained an initial small molecule which is co-crystallized with the target protein, and the binding site of this small molecule can be used as the active site.

After the three dimensional structure of the target molecule is obtained and the small molecule binding site is located, a good lead compound is designed or searched from synthesis (de novo design) or from compound database (virtual screening). The binding and scoring of this lead compound is evaluated and those with high binding energies can be experimentally tested as possible lead compound.

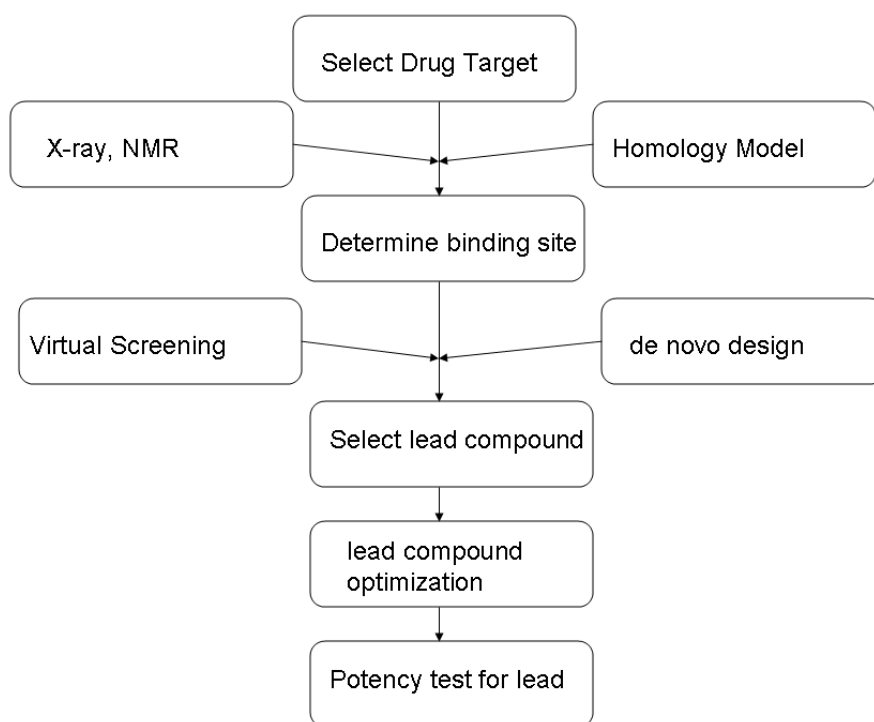


**Figure 1.1** Schematic process of structure-based drug design

## 1.2 Outline of Subsequent Chapters

In Chapter 2 and Chapter 4, docking and scoring are performed on PTX binding to human and mouse MD-2,[7] and also worked on LPS binding to human TLR4/MD-2 dimer with or without KDO moiety. The docking results explained bio-activity differences based on the experiment results. In Chapter 3, protein-protein docking methodology, Rosetta, was adopted to find the TLR4/MD-2 dimerization model. In Chapter 5, a quantum calculation related project is described. Chapter 6 and 7 describe the applications of the structure based drug design in two specific cases, histone lysine methyltransferase

(H3K9me2) inhibitor design [8, 9] and Chemokine Receptor Type 4 (CXCR4) inhibitors design.

## Chapter 2

### Paclitaxel binding to Human and Mouse MD-2

#### 2.1 Introduction

Paclitaxel (PTX, **Figure 2.1**) is a potent anti-cancer agent derived from the Pacific yew tree which acts through over-stabilization of cellular microtubules. The natural product leads to disruption of mitotic machinery and inhibition of cell growth.[10-12] Structurally, the PTX molecule and its interaction with  $\beta$ -tubulin have been well-characterized.[13-15] PTX also exhibits anti-angiogenic properties, and these have expanded the application of the family of drugs known as taxanes to a variety of tumor types (breast, prostate, ovarian, lung) [16] and to treatment of coronary atherosclerosis via paclitaxel coated coronary stents. [17] The contribution of innate immunity pathways to the mechanism of action of PTX has not been well-studied. However, the wide-ranging applications of this family

---

of drugs and the known interaction of PTX with toll-like receptor 4 (TLR4)[18, 19] suggest a potential anti-inflammatory mechanism for some of the observed biological effects. TLR4 is a critical component of the innate immune response to bacterial endotoxins. [20, 21] Activation of TLR4 by endotoxin requires association with the accessory protein MD-2, an *N*-glycosylated [22] 19-27 kilo-Dalton protein that is expressed in both a soluble and a membrane bound form. [23] Binding of endotoxin (lipopolysaccharide [LPS] or lipooligosaccharide [LOS]) to MD-2 in association with TLR4 can lead to dimerization or oligomerization of two or more TLR4 receptors and subsequent cellular activation.[24, 25] Although much is known about the MD-2 protein, its interaction with TLR4, and the hypothesized binding site of MD-2 for endotoxin, [26-30] the specific structural requirements of endotoxin and other TLR4 ligands for MD-2 association and TLR4 activation are not fully understood.

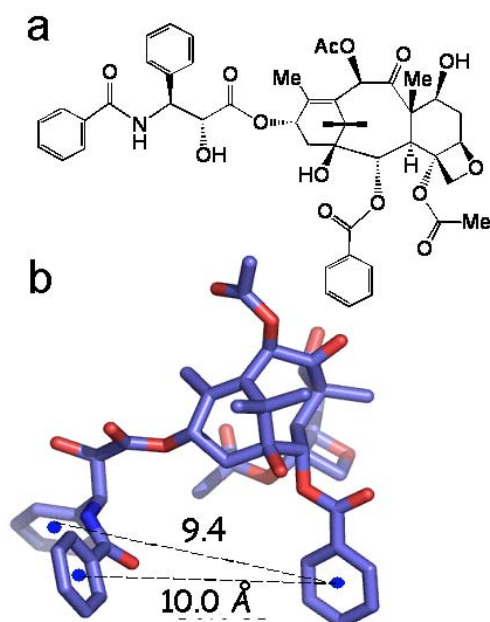


**Figure 2.1 Paclitaxel.** (a) Topological structure of PTX. (b) 3-D conformation of PTX as observed in  $\beta$ -tubulin (i.e. T-Taxol). This conformer is one of the many possible options for PTX binding to MD-2 as revealed by Glide docking.

MD-2 belongs to a family of proteins which express an ML (MD-2-related lipid-recognition) domain. [31] The protein contains 150 amino acids which form a “clamshell” binding site (**Figure 2.2**) for hydrophobic ligands inserted between two  $\beta$ -pleated sheets. [31, 32] These proteins include MD-1 associated with RP105 on B cells; the dust mite antigens, Der p2[33] and Der f2; [34] Niemann-Pick disease C2 (NPC2); [35] and the GM2-activating protein important in Tay-Sachs gangliosidosis. [36, 37] Der p2 exhibits the most homology to MD-2, and its NMR-determined solution structure includes a  $\beta$ -folded binding

pocket for an unidentified lipid ligand. [32, 34] MD-2 is thus predicted to directly interact with the lipid A of endotoxin. Several important crystal structures have been published recently (human MD-2 bound to the TLR4 antagonist, lipid Iva;[38] the human TLR4-MD-2 complex associated with the endotoxin antagonist eritoran; and mouse MD-2 complexed to mouse TLR4[39]). These enhance our understanding of the structure of MD-2 greatly, while offering an opportunity to explore the interaction between MD-2 and various TLR4 agonists and antagonists.

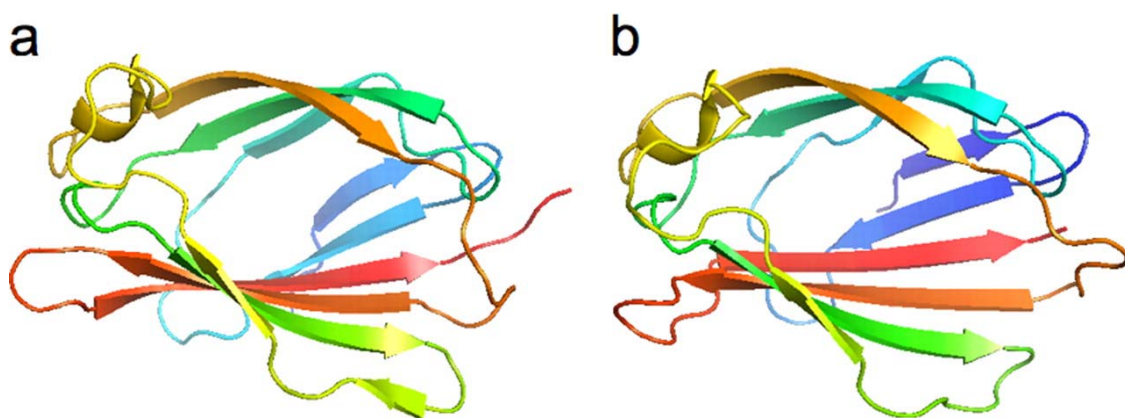


**Figure 2.2 MD-2 structures.** (a) hMD-2 crystal structure, ligand removed (Protein Data Bank code 2Z65). (b) mMD-2 crystal structure (Protein Data Bank code 2Z64).

**MD-2 confers species-specific ligand recognition.** The species-specific discrimination of TLR4 ligands by MD-2 is exemplified by PTX, a pro-inflammatory murine TLR4/MD-2 ligand. Murine MD-2 binding to paclitaxel is an essential step for species-specific activation of the mouse TLR4

---

with subsequent inflammatory cytokine response [18, 40, 41]. As demonstrated by chimeric experiments in which human TLR4 was expressed with mouse MD-2, activation of TLR4 by PTX requires the mouse MD-2 protein and is independent of TLR4 species [18, 41]. Species-specific activation of the mouse TLR4 receptor complex by *Salmonella enterica* lipid A has also been described by Muroi et al[42] and is dependent upon MD-2 rather than TLR4.

Recombinant human MD-2 (rhMD-2) produced in a *Pichia pastoris* expression system is able to confer responsiveness on TLR4 expressing cells and bind to meningococcal endotoxin.[43] We show that rhMD-2 also binds PTX in a dose-dependent fashion, but the TLR4 receptor is not activated. In an attempt to understand the activation event, we have employed the recently reported crystal structures of rhMD-2 and mMD-2 to construct models of the interactions between PTX and these proteins. Differences in MD-2 electrostatic potential surfaces, hydrophobicity, binding pocket size and a mouse *versus* human conformational gating of the 123-130 loop are predicted to be responsible for the species-specific activation of TLR4 by PTX.

## 2.2 Computational Method

### 2.2.1 Homology Modeling

A homology model of mouse MD-2 was constructed by application of Prime v1.6 with the Maestro interface (Schrödinger, LLC) and by using the crystal structure of hMD-2 complexed with lipid IVa (PDB code 2E59; 79% sequence similarity)[38] as template. The resulting homology model was refined by backbone and side chain energy optimizations using the OPLS force field within Prime. A WHATIF analysis demonstrated very similar Z-scores between the mMD-2 homology model and the hMD-2 crystal structure in terms of 1<sup>st</sup> and 2<sup>nd</sup> generation packing quality, chi-1/chi-2 rotamer normality, and backbone conformation.

### 2.2.2 Computational Ligand-Protein Docking

*Glide Docking.* Previously established “NAMFIS” conformations of PTX [44] were docked separately into the cavity regions of the human MD-2 crystal structure (PDB code 2E59)[38] devoid of lipid IVa and the mMD-2 homology model described above using Glide with SP precision (Schrödinger, LLC). This methodology regards the structure of the protein as a rigid body, but treats the ligand as a conformationally flexible molecule. The same PTX conformers were similarly docked into the ligand-free MD-2 X-ray structures derived from the hybrid-TLR4-hMD-2-Eritoran complex (PDB code 2Z65) and the

---

mTLR4-mMD-2 complex (PDB code 2Z64).[39] Unlike the binding of PTX to  $\beta$ -tubulin,[13] neither MD-2 docking exercise led to NAMFIS conformations as the favored binding pose. Glide was also used to examine the relative energies of PTX docked to the external surfaces of the MD-2 proteins.

*Induced fit docking.* To improve the fit between protein interior and PTX and to achieve deeper residence of the ligand within the cavity, induced fit docking with Prime v1.6 (Schrödinger, LLC) was performed. This approach allows both protein side chain movement and ligand flexibility. Duplicate poses were removed with MacroModel (Schrödinger, LLC), and the resulting MD-2/PTX complexes were sorted energetically with the MMGBSA scoring algorithm.[45]

### 2.2.3 Molecular Volumes

The ligand volumes were calculated by extracting the structures from their respective protein X-ray or EC (electron crystallographic; e.g. PTX T-Taxol conformation) complexes as pdb files followed by importing into the Spartan software. A single point energy calculation provides the volume of the corresponding CPK model. The volumes of the MD-2 cavities were obtained by the web-based CASTp package.

---

## 2.3 Results and Discussion

### 2.3.1 MD-2 models and Glide Docking

Paclitaxel (molecular weight of 854) is a globular hydrophobic molecule with a molecular volume of  $831 \text{ \AA}^3$  in its microtubule binding conformation.[46] By comparison, lipid IVa, with a molecular weight of 1405 and a molecular volume of  $1451 \text{ \AA}^3$ , is a highly flexible structure that can adopt a flat and laminate-like shape for its four lipid appendages. In principle, both ligands can occupy the MD-2 pockets since the cavity volumes for human (X-ray)[38] and mouse (homology model) MD-2 are  $1622 \text{ \AA}^3$  and  $1683 \text{ \AA}^3$ , respectively. Attempts to dock PTX into either of the two proteins with Glide lead to complexes in which the ligand rests at the mouth of the cavities, but does not penetrate within. The entrance passages into both mouse and human MD-2 are clearly too small to accommodate the globular ligand.

During the course of this work, several additional MD-2 crystal structures were released: hybrid-TLR4-hMD-2-Eritoran complex (PDB code 2Z65) and mTLR4-mMD-2 complex (PDB code 2Z64).[39] The MD-2 proteins revealed CASTp[47] pocket volume prediction estimates of  $1906$  and  $1922 \text{ \AA}^3$ , respectively. The cavity volumes have increased by almost  $300 \text{ \AA}^3$  relative to that for the hMD-2/lipid IVa complex, suggesting a significant change in protein conformation. Interestingly, superposition of hMD-2-lipid IVa (PDB code

---

2E59)[38] and hMD-2-eritoran (PDB code 2Z65)[39] illustrates that the backbones overlay quite well, but several side chains near the cavity entrance adopt different orientations. Particularly critical for LPS docking are the Arg90 and Glu92 residues located in this vicinity. The residues are substantially altered in their spatial orientations in the two human MD-2 crystal structures.

The X-ray structures of both lipid IVa and eritoran bound to hMD-2 show that, while the lipid moieties of the molecules extend deep into the protein cavities, the sugar phosphate groups remain in solution outside the mouth of the cavities (**Figure 2.2a**). At the same time, as pointed out previously, residues around the pocket entrance assist in anchoring the ligand to the protein. In the case of lipid IVa (2E59), interactions on both lips of the mouth clamp the ligand in place. **Figure 2.3a** illustrates Lys122 interacts electrostatically with both phosphates at NH---O distances of 4.2 and 5.6 Å. On the opposite lip, Arg90 sustains similar NH---O separations of 4.7 and 5.4 Å, while simultaneously associating with Glu92 (4.5 Å). Eritoran, on the other hand, makes use of the charged residues on only one lip of the cavity opening as depicted by **Figure 2.3b**. Both Lys122 and Lys125 participate in local contact with the sugar phosphates (4.4-6.3 Å), but Arg90 and Glu92 do not associate with the ligand. Instead, again as electrostatic partners, the two residues are directed conformationally away from the mouth and reside in aqueous solvent. The different arrangement of MD-2 side chains for the lipid IVa and eritoran TLR4 antagonists can be described to variations in the lipid sizes emanating from the sugars at the heads of the structures. Lipid IVa

possesses four C<sub>14</sub> extensions, while eritoran displays two C<sub>10</sub> and single C<sub>14</sub> and C<sub>18</sub> hydrocarbon chains. As a result, the folding organization of these chains in the MD-2 pocket causes different positions of the heads of the ligands just outside the pocket with concomitant interactions shown in **Figure 2.3**.

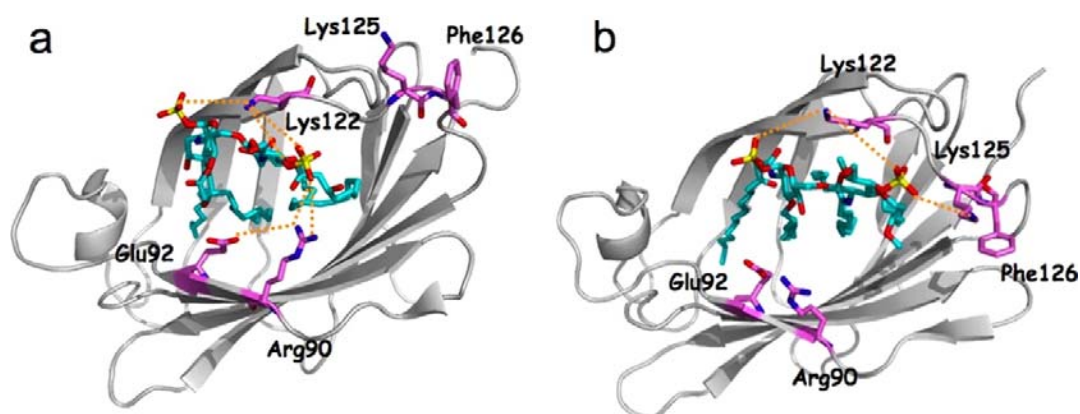


**Figure 2.3 Lipid molecules in hMD-2 bind differently to the cavity mouth. (a)** lipid IVa in hMD-2 (Protein Data Bank code 2E59) clamped by Lys<sup>122</sup> at the upper lip of the cavity mouth and by Arg<sup>90</sup> and Glu<sup>92</sup> at the lower lip. **(b)** eritoran in hMD-2 (Protein Data Bank code 2Z65), illustrating columbic interactions with Lys<sup>122</sup> and Lys<sup>125</sup> on the upper lip but no interactions with Arg<sup>90</sup> and Glu<sup>92</sup>

The implication of conformational mobility around the MD-2 entrance channel is significant. Glide docking of PTX into hMD-2-eritoran (2Z65) illustrates that the molecule docks almost completely within the binding cavity. The basis for the docking differences between MD-2/2E59 and MD-2/2Z65 can be traced largely to the Arg90 and Glu92 partners. Adjustment of the side chain

---

torsion angles of the single Arg90 residue in hMD-2-lipid IVa to the values in hMD-2-eritoran increases the cavity volume by 100 Å<sup>3</sup>. Re-orientation of nearby Glu92 similarly leads to a total volume increase of 200 Å<sup>3</sup>, indicating that these two residues alone appear to control access to the cavity. As a result, the entrance of human MD-2 opens up sufficiently to fit PTX in the pocket very similar to that observed for the MD-2 protein in X-ray structure of 2Z65/eritoran.

PTX was likewise subjected to docking into mMD-2 from the mTLR4-mMD-2 complex (2Z64) with a similar but not identical result relative to the human protein. Although the overall backbones of the human and mouse MD-2 structures (2Z65 and 2Z64, respectively) are essentially superimposable, the properties of the individual surfaces display important differences. Comparison of the electrostatic surfaces show that the cavities for both structures are close to electroneutral, but the outer edge of mMD-2 is more electronegative than hMD-2, especially in the Cys95 – Cys105 loop, which is critical for the MD-2/TLR4 interaction.[39] Furthermore, the electrostatic surface of human MD-2 displays three electropositive patches corresponding to Lys58, Lys122, and Lys125, which are absent on the mouse MD-2 surface. The electrostatic discrepancy in this peptide segment is predicted to be partially responsible for the differences in the mouse and human docking surfaces. (**Figure 2.4**) The increased negative electrostatic potential of the external surfaces of the mMD2 relative to hMD2 may be of significance in protein-protein interactions. While both cavities appear to have similar hydrophobic properties (not shown), certain specific

regions on the external surface of mMD-2, particularly Phe126, contribute hydrophobic character which may be responsible for species-specificity. (**Figure 2.5**)

Importantly, although given ample opportunity, none of the top 50 poses arising from Glide docking into h2Z65 and m2Z64 were found outside the pockets of the MD-2 proteins. Certain PTX conformers not in the top 50 poses were docked on the outer surfaces, but the energies derived from the Glide scoring function were considerably higher than poses within the pocket. Thus, for MD-2 proteins in the absence of contact with TLR4, we regard such ligand-protein interactions as low probability.

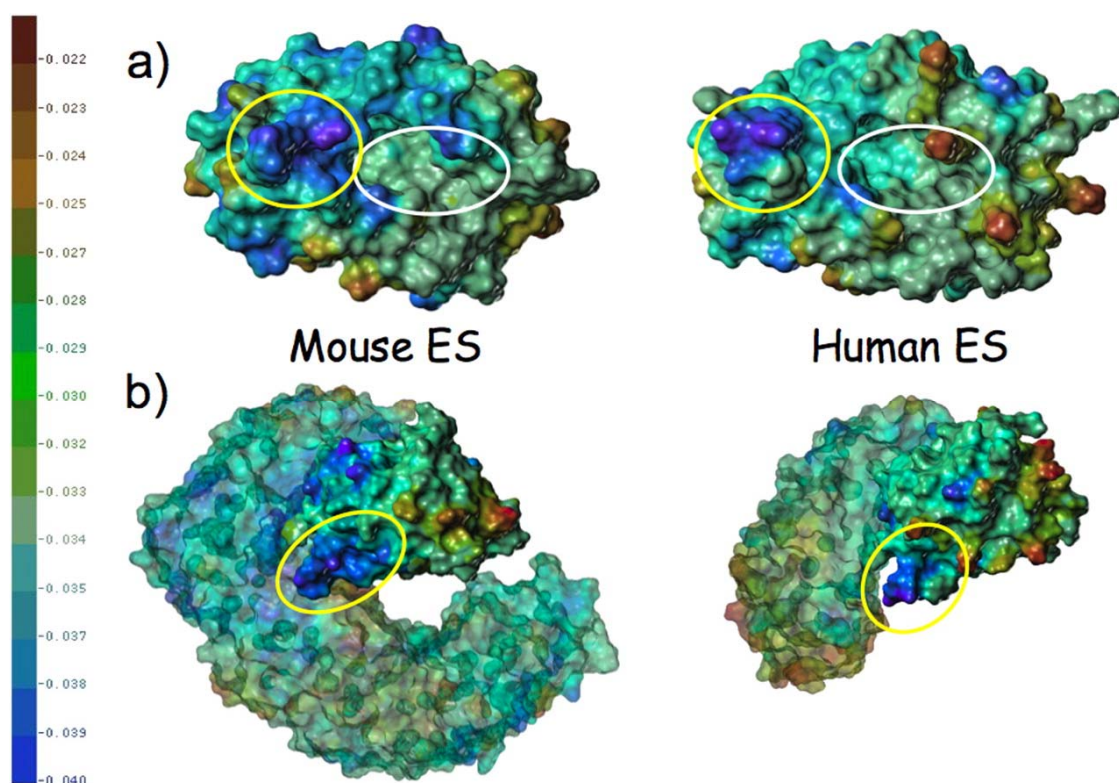
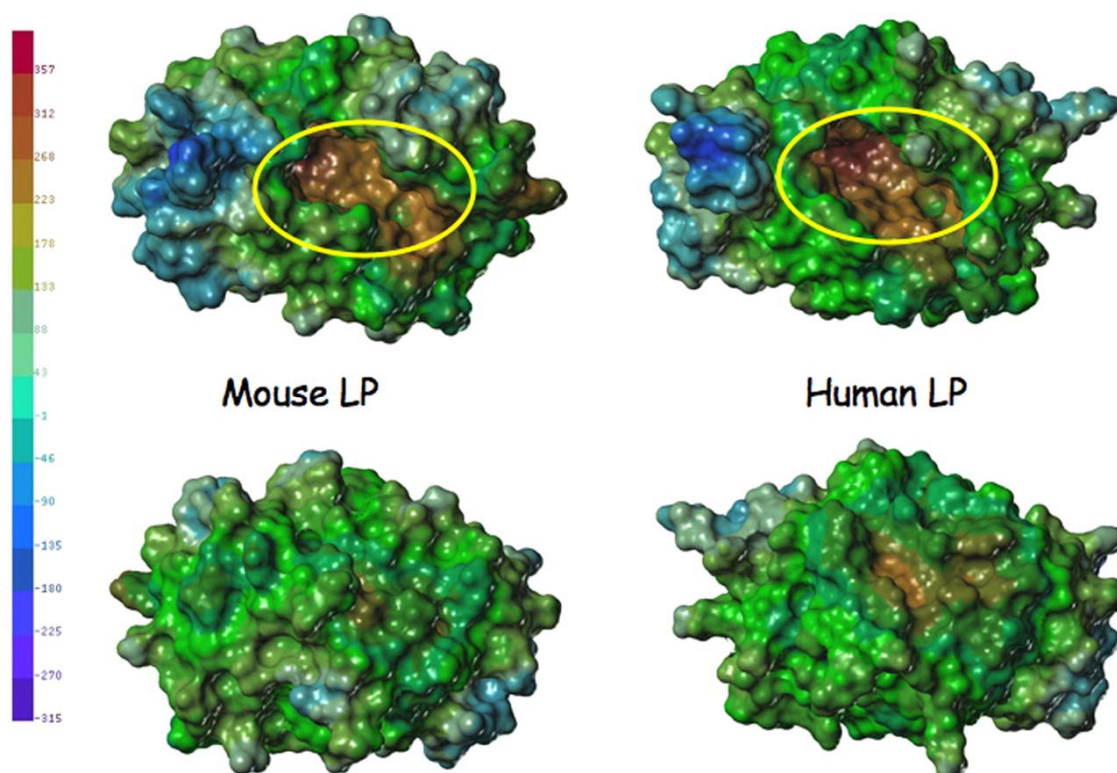


**Figure 2.4 Electrostatic potential energy surfaces of MD-2 and MD-2·TLR4 models.** *Left, mouse; right, human.* (a) Electrostatic surfaces (*blue is negative*) of the MD-2 proteins in the MD-2·TLR4 x-ray complexes (m2Z64 and h2Z65) were produced with SYBYL software. The surfaces are shown with the binding cavities *circled in white* and the Cys<sup>95</sup>-Cys<sup>105</sup> loops in *yellow*; (b) complexes of MD-2·TLR4 in which the MD-2 is pictured to the *right* of each *graphic* as a solid surface, whereas the TLR4 protein is shown as *translucent*. The corresponding Cys<sup>95</sup>-Cys<sup>105</sup> loops are *circled in yellow*. In the human MD-2·TLR4 complex, the latter loop is not in direct van der Waals contact with TLR4 residues.



---

**Figure 2.5 Lipophilic and hydrophobic surfaces of the MD-2 models.**

Lipophilic (*LP*; *blue*) and hydrophobic (*brown*) surfaces of MD-2 (2Z64 and 2Z65) were obtained with SYBYL software. The surfaces are shown from the front (*top*; cavities are *circled* for clarity) and from the back (*bottom*).

**2.3.2 Induced Fit Docking of PTX into MD-2**

Results from induced fit docking of PTX to h2Z65 (Green) and m2Z64 (Blue) are shown in **Figure 2.6a**. Side chain movements around the cavity opening, resulting from the induced-fitting procedure, cause a slight expansion of the entry channel relative to the X-ray structure (Induced fit cavity volumes for h- and mMD-2 are 1945 and 1933 Å<sup>3</sup>, respectively). One of these, involving Phe126 as shown in **Figure 2.6b**, portrays a PTX docking pose for h2Z65. From the most favorable docking poses in **Figure 2.6a**, comparison of human and mouse MD-2 illustrates that although the bulk of PTX's baccatin core occupies a similar position in the cavity, the two C-13 phenyl groups extend in different directions. This may be a clue to the basis of the opposite performances of PTX in activating the TLR4 signal. In the hMD-2 top pose, the benzamido phenyl group (NHC(O)Ph) is very close to Phe126, suggesting that a hydrophobic interaction may exist between them. In addition, the (CH<sub>2</sub>)<sub>4</sub> moiety of the Lys125 side chain appears to associate with this phenyl ring by hydrophobic contact. The C-13 phenyl group in PTX exhibits a  $\pi$ -cation interaction with Lys122, since the terminal NH<sub>3</sub><sup>+</sup> group is directed toward the plane of the phenyl group at an

---

NH---C distance of only 2.6 Å. In addition, three intermolecular H-bonds serve to anchor the ligand into the protein as depicted in **Figure 2.7**. The apparent electrostatic association of PTX with MD-2 contrasts with the largely hydrophobic binding demonstrated by PTX in  $\beta$ -tubulin.[13] In MD-2, the multiple interactions attract the Gly123-Lys130 loop so as to form a concave surface facing the docked PTX.

The same loop in the mouse protein is oriented in the reverse direction. We wondered if PTX occupation of the mouse MD-2 cavity might not only favor an outward directed loop, but also extend it further. Comparison of the most favorable mMD-2 docking pose with the mMD-2 crystal structure reveals that loop 123-130 experiences movement outward as a consequence of PTX binding as depicted in **Figure 2.8**.

It is important to point out that the residues in the critical LPS recognition sequence Phe119-Gly123 are conserved in all species of MD-2 except Lys122. In our exploration of the PTX occupation of the MD-2 cavity, this residue plays a crucial role for both hMD-2 and mMD-2 as reflected by **Figure 2.3**. However, in the mouse protein, position 122 is occupied by Glu instead of Lys. Thus, the absence of a  $\pi$ -cation interaction (**Figure 2.6b**) between PTX and Glu122 in the mouse-PTX complex causes an entirely different binding pose for PTX resulting in a qualitatively dissimilar interaction between the ligand and the Gly123-Lys130 loop. The loop dislocation suggested by **Figure 2.8** is accommodated by this

observation. As we discuss below, movement of the loop is most likely necessary for TLR4 dimerization and activation.

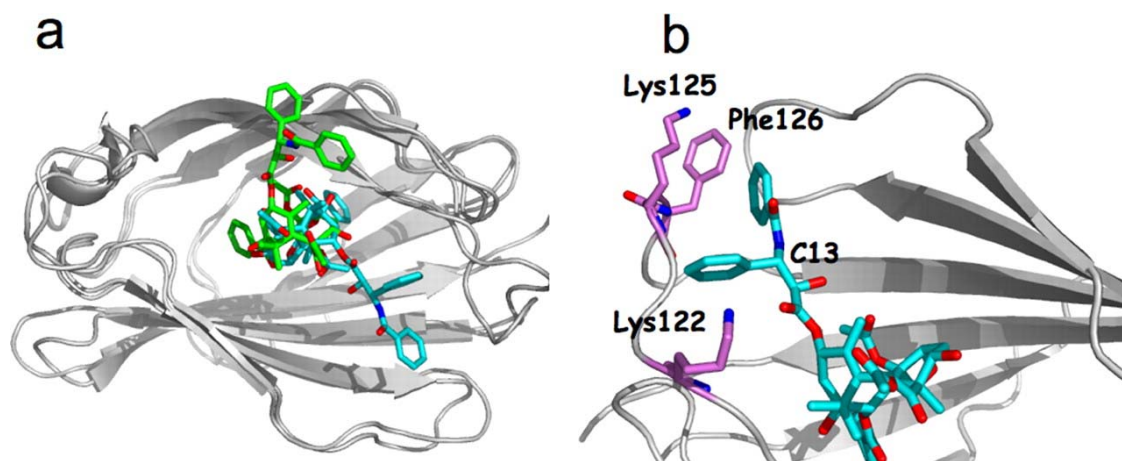


**Figure 2.6 MD-2·PTX docking poses** (a) the top docking poses for PTX in mouse MD-2 (*green*) and human MD-2 (*blue*) (Protein Data Bank codes 2Z64 and 2Z65, respectively); (b) detailed view of the top PTX docking pose in human MD-2 (Protein Data Bank code 2Z65) illustrating the Phe<sup>126</sup>-benzamido phenyl hydrophobic interaction and the Lys<sup>122</sup>-C13 phenyl  $\pi$ -cation interaction.

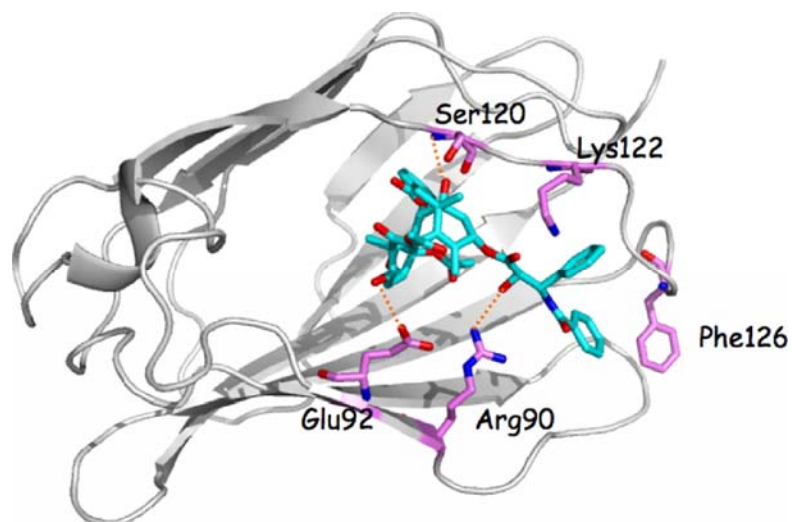


**Figure 2.7** Detailed view of the top PTX docking pose in human MD-2 (Protein Data Bank code 2Z65) illustrating hydrogen bonds for Ser<sup>120</sup>-C1 hydroxyl, Glu<sup>92</sup>-C7 hydroxyl, and the Arg<sup>90</sup>-C13 hydroxyl.

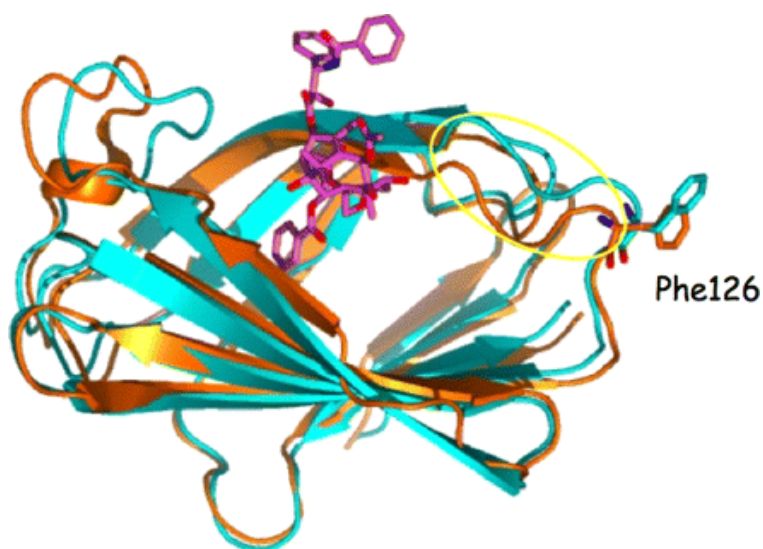


**Figure 2.8** Comparison between mMD-2 top docking pose (*blue*) and mMD-2 crystal structure (*orange*). PTX docking shifts the 123-130 loop (*circled in yellow*), including Phe<sup>126</sup> outward (*blue*) relative to the crystal structure.

### 2.3.3 Discussion

Although the anti-cancer mechanism of action of PTX has long been attributed to effects at the level of  $\beta$ -tubulin, growing evidence supports innate immune activation and possibly anti-tumor effects of PTX mediated through TLR4/MD-2. [19, 48] The LPS mimetic activity of PTX in murine systems has been extensively documented. [18, 40, 41] Activation of the TLR4/MD-2 pathway by PTX has been demonstrated using murine macrophages, [49-51] transfected cell lines [18, 40] and mouse cancer cell lines.[52] Further, C3H/HeJ cells, which are known to be unresponsive to LPS due to a mutation in the *tlr4* receptor gene, fail to respond to PTX. [53] In contrast, cells transfected with human TLR4 and human MD-2 fail to mount a pro-inflammatory response to PTX. [18, 40] The species-specific difference is attributed to the MD-2 protein. [41, 54]

This study demonstrates that although PTX does not induce a pro-inflammatory cytokine response through human MD-2, binding to human MD-2 does occur. Recombinant human MD-2, which confers responsiveness to endotoxin with human TLR4-expressing cells (data not shown), bound PTX in a dose-dependent fashion, and binding was inhibited by an anti-human MD-2 antibody. Further support for PTX binding to human MD-2 was furnished by molecular modeling that compares the docking probabilities of PTX in the human MD-2 molecule to that in the mouse MD-2 protein. These two proteins share 67% identity at the

---

amino acid level, and both are necessary for activation of TLR4 by bacterial endotoxin, yet they discriminate PTX as a TLR4 ligand. As elaborated below, discrimination may be traced, in part, to sequence variations that result in conformational differences between the proteins accompanied by alterations of surface charge distribution (i.e. electrostatic potential), binding pocket size and location of PTX binding within the MD-2 pocket which results in reorganization of the 123-130 loop.

The present study demonstrates that although PTX does not induce a pro-inflammatory cytokine response through human MD-2, binding to human MD-2 does occur. Recombinant human MD-2, which confers responsiveness to endotoxin with human TLR4-expressing cells (data not shown), bound PTX in a dose-dependent fashion, and binding was inhibited by an anti-human MD-2 antibody. The observation that PTX associates with human MD-2 *in vitro* without promoting TLR4 activation is in strong contrast with the action of PTX on mouse MD-2/TLR4. With the help of molecular modeling, we propose an explanation for the species-specific differences in the pro-inflammatory TLR4-mediated response by this drug. It rests on the recent model for TLR4-MD-2 aggregation by Kim *et al.*, [39] which highlights the function of Phe126 as a bridge to connect MD-2 and TLR4 proteins leading to formation of a dimer. In the present study, PTX binding to human MD-2 is characterized by a  $\pi$ -cation interaction with Lys122 and hydrophobic interaction with Phe126, causing the latter to reside inside the pocket. The electrostatic and lipophilic properties of hMD-2 likewise

---

illustrate the positive character of Lys122 (**Figures 2.5 and 2.6**), while emphasizing burial of Phe126 within the hydrophobic cavity (**Figures 2.3b, 2.6b and 2.7**). In the mMD-2 case, the positively charged patch on the outer surface is absent; the hydrophobic orientation for Phe126 is directed away from the protein; and loop 123-130, the bridge for TLR4 dimerization, forms a convex surface to facilitate oligomerization (**Figure 2.8**). Since one commonly accepted sequence of events believed to activate TLR4 includes the binding of a ligand (i.e. PTX) to soluble MD-2 followed by binding of the PTX-MD-2 complex to TLR4, subsequent homodimerization of TLR4 and signal transduction, [55, 56] TLR4 dimerization is an indispensable step in signal propagation. However, PTX lacks interaction with loop 123-130 in mMD-2. Thus, in this isoform of the enzyme, PTX does not appear to have the capacity to draw the loop inside the mouth of the pocket, sequester Phe126 and thereby prevent the TLR4/MD-2 complex dimerization.

It is noteworthy that in the model of mMD-2 bound to PTX, loop 123-130 is forced outward with a concomitant change in the conformation of Phe126 (**Figures 2.8 and 12**). This dynamic process might serve as the primary step for TLR4 dimer formation upon PTX docking. This line of reasoning suggests the hypothesis that agonist binding to mMD-2 may cause a similar conformational change in mMD-2 to facilitate homodimer formation. The recently disclosed X-ray crystal structure of hMD-2 bound by lipid IVa supports this hypothesis. As pointed out by the authors of the work, insertion of two additional acyl chains into

the hydrophobic cavity (e.g. lipid A) would lead to enlargement of the protein cavity, most certainly accompanied by reorganization of loop 123-130, and give rise to subsequent signal propagation. Thus, the MD-2 binding of molecules with varying molecular volumes can be expected to promote different local conformational changes in the protein as illustrated for lipid IVa, eritoran and PTX above. In addition, much bulkier molecules, such as the lipid A and other LPS agonists, require a flexible binding pocket in order to fully penetrate the protein.

Species-specific differences in signaling influenced by the binding geometry of PTX to MD-2 are predicted to effect activation of TLR4 at the level of its ectodomain and recruitment of downstream effector molecules. Differential TLR effector molecule signaling in response to traditional ligands has been described. [57, 58] Further, new TLR ligands with anti-cancer and apoptotic effects have been identified, further supporting the potential for a TLR4-mediated anti-cancer mechanism of PTX. [59-61] The binding of PTX to human MD-2 supports a role for the innate immune response to PTX in the human system and may uncover a new mechanism of action for this important family of anti-cancer and anti-inflammatory agents.

## Chapter 3

### TLR4/MD-2 dimerization Model

#### 3.1 Introduction

Lipopolysaccharide molecules are complex glycolipids that form the outer layer of the outer membrane of Gram-negative bacteria [62]. The lipid A domain of LPS is responsible for cellular activation and consists of a disaccharide and acyl chains of variable length and number. [63] A small difference in LPS, such as length or number of acyl chains, has a great influence on host response against Gram-negative bacteria. [64] *Escherichia coli* lipid A is usually hexa-acylated whereas a tetra-acylated lipid A, lipid IVa, is also produced by *E. coli* as an intermediate in the lipid A biosynthetic pathway. [63] Although, hexa-acylated lipid A stimulates the immune response, lipid IVa was originally identified as an inhibitor of the human LPS receptor and was considered a candidate to be developed for clinical use as an endotoxin antagonist. Excessive responses to the endotoxic LPS frequently result in severe sepsis, a rapidly progressing

---

inflammatory disease, which is the 10th leading cause of death in USA. [65]

The TLR4 pathway activates the key transcriptional regulator NF- $\kappa$ B, resulting in the production of inflammatory cytokines. A commonly accepted sequence of this pathway includes: a LPS-binding protein (LBP) binds Gram-negative bacteria to extract LPS from the cell wall and delivers an LPS monomer to CD14; [66] LPS/LBP binds to CD14, the second accessory molecule needed for LPS sensing; myeloid differentiation-2 (MD-2), as a co-receptor for TLR4, forms the complete recognition site for LPS; [67, 68] and finally, LPS binding to TLR4/MD-2 triggers dimerization of TLR4 which stimulates the intracellular pathway that ultimately leads to activation of NF- $\kappa$ B and the production of pro-inflammatory cytokines.[69] Of particular importance, MD-2 plays a key role in lipid A recognition whereas TLR4 is thought not to participate directly in lipid A binding. [70]

Several important crystal structures have been published recently (human MD-2 bound to the TLR4 antagonist, lipid IVa; [38] the human TLR4-MD-2 complex associated with the endotoxin antagonist eritoran and mouse MD-2 complexed to mouse TLR4 [39]). These enhance our understanding of the structure of MD-2 and TLR4 and also offer an opportunity to explore the interaction between MD-2 and various TLR4 agonists and antagonists. However, the conformation of the TLR4-MD-2 homodimer is still unclear. Here, we will apply a computational method to predict this homodimer model.

## **3.2 Computational Methods**

### **3.2.1 Homology Modeling**

Up to now, the crystal structure of human TLR4 is a hybrid one, which contains a part of the human TLR4 (N-terminal) and another LRR protein TV3. (PDB code: 2Z65) This incomplete human TLR4 structure could not be used in protein-protein docking. As a result, a homology model of the whole human TLR4 structure based on mouse TLR4 is required. Sequences were aligned with CLUSTALW.[46] Homology modeling of human TLR4 sequence to template (mouse TLR4) was performed using the application Prime v 2.0 within the Maestro interface (Schrödinger, LLC). The homology model was refined by backbone and side chain energy optimization using the OPLS force field within Prime. The resulting model of human TLR4 was evaluated by PROCHECK. MOLCAD, within SYBYL v 7.0 (Tripos, Inc.), was used to define Fast Connolly van der Waals surfaces to which electrostatic (Tripos force field) and lipophilic [71] properties were mapped for this protein model.

### **3.2.2 Protein-Protein Docking**

Human (homology) and mouse (crystal) TLR4-MD-2 dimers were predicted by Rosetta protein-protein docking. The manually docked model was used as a starting point for sampling the surrounding free energy landscape by using

manyindependent Monte Carlo minimization trajectories according to a RosettaDock protocol [72]. Briefly, the rigid degrees of freedom of the starting model are randomly perturbed, and the perturbed model is subjected first to low-resolution refinement and then to high-resolution refinement. In the latter high-resolution step, the side chain and backbone degrees of freedom are optimized simultaneously in the context of a detailed all-atom energy function dominated by short-range hydrogen bonding, van der Waals interactions, and desolvation. The complete conformational space starting with 1000 different random orientations was sampled in this global docking search.

### **3.3 Results and Discussion**

Sequence alignment by CLUSTALW showed that the sequence identity for human and mouse TLR4 is 62% at the amino acid level. Following this alignment, a homology model of human TLR4 was constructed based on the crystal structure of mouse TLR4 (PDB code: 2Z64) as the template. After backbone and side chain energy optimization refinement, the homology model was evaluated by PROCHECK analysis, which showed a significantly improved Ramachandran plot, having more hydrophobic residues in the core. In addition, this homology model eliminated bad contacts between amino acids. However, the main-chain parameters for the model showed one unfavorable parameter, while in mouse TLR4 crystal structure, no such parameters exist.

After the crystal structures of human MD-2 and mouse TLR4 complexed with mouse MD-2 were released, the dimerization model of TLR4/MD-2 triggered a lot of interest. In 2007, Kim et al. proposed three models of the LPS-induced TLR4-MD-2 dimerization. The first model shows the one MD-2 in direct contact with the other MD-2 through Phe126. The second one shows that LPS binding to MD-2 induces a structural change in TLR4 and promotes direct dimerization of TLR4 molecules. And in the last model, LPS binding induces a structural change in the Phe126 edge of MD-2 that promotes interaction between the edge and the central or C-terminal domain of a second TLR4. Model-3 is preferred, based on experimental results: the receptor dimerization requires the central and/or C-terminal domain of TLR4, while Phe126 and His155 mutants of the MD-2/TLR4 complex were not dimerized by LPS.[39] (**Figure 3.1**)

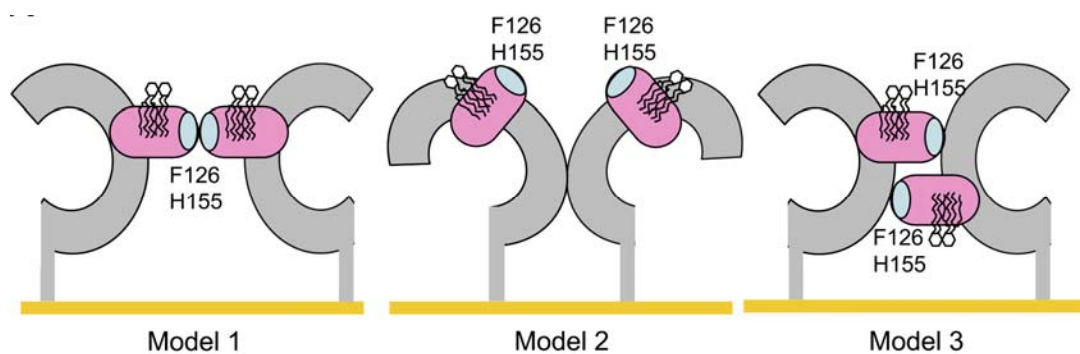


**Figure 3.1** Three models of the TLR4-MD-2 dimer are shown. MD-2 and TLR4 are colored in magenta and gray, respectively. The yellow bars represent the cell membrane.

Based on these evaluations of the proposed models, model-3 was manually built for mTLR4/mMD-2 and hTLR4(homology model)/hMD-2 as the starting geometries. Rosetta protein-protein docking (Global docking) was performed to search possible binding modes for this homodimer. 1000 results were generated for each of the homodimers and were sorted by an energy score, which is mainly determined by shape complementarities and electrostatic interactions.

The best result for mouse closely resembles model-3 as proposed: the interaction of MD-2 and TLR4 is through Phe126 edge and the C-domain of TLR4. If we look at the detailed view, it shows that Asn26, Arg55, Phe126 and His155 are all candidates located at the interface between MD-2 and the TLR4, each of which can interact with the residues in the TLR4 (**Figure 3.2**). And also, the lowest distance between mMD-2 (through His155) and mTLR4 (through Asn484) is 4 Å.

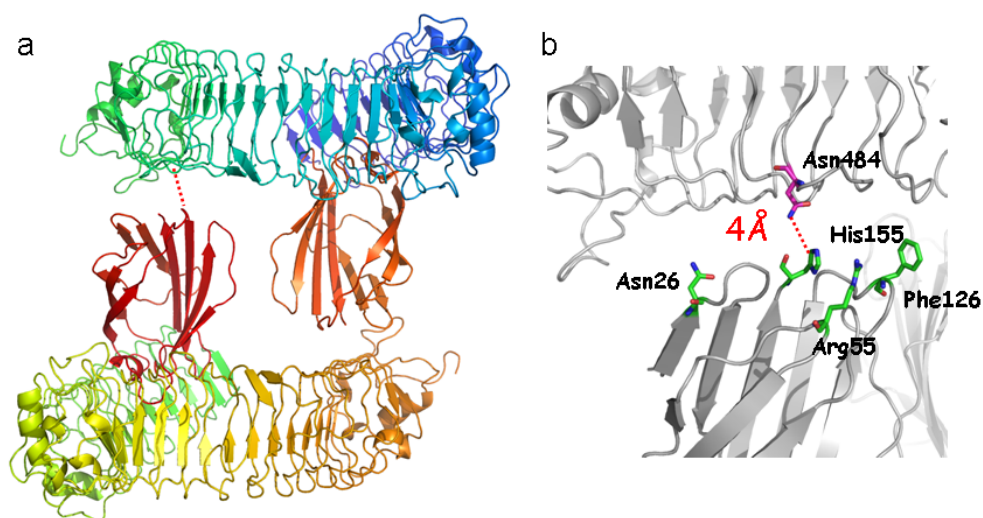


**Figure 3.2** (a) the mouse TLR4-MD-2 homodimer are shown in the diagram; (b) Detailed view of the interface between MD-2 and TLR4. The green residues are Asn26, Arg55, Phe126 and His155.

On the whole, the best dimer model for human is similar to the mouse result. However, the mouse TLR4-MD-2 homodimer associates more tightly than the human one, since comparison of the human and mouse dimer models shows that mouse MD-2/TLR4 structure is more compact (**Figure 3.3b**). The detailed view shows that Ser28, Lys55, Lys128 and Gln155 are candidates located at the interface between MD-2 and TLR4, which can interact with residues in TLR4, and the lowest distance between hMD-2 (through Lys128) and hTLR4 (through Lew574) is 6Å. (**Figure 3.3a**)

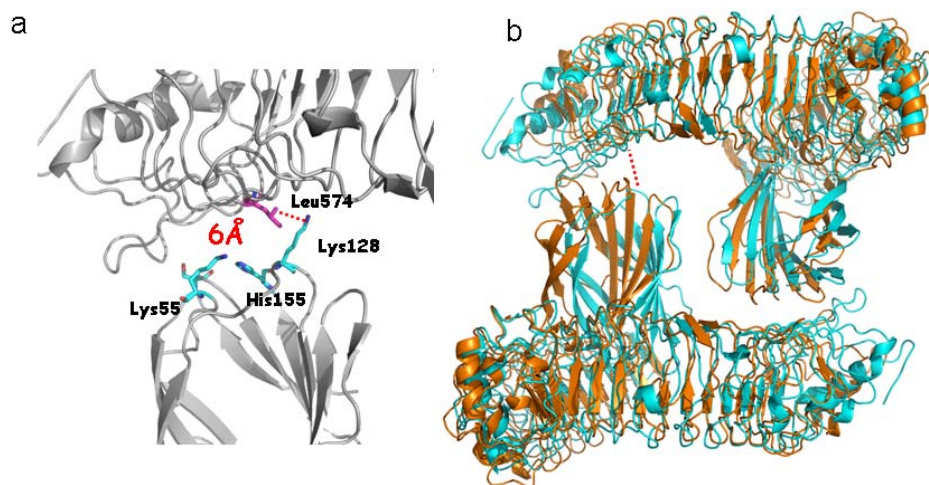


**Figure 3.3** (a) The detailed view of the interface between MD-2 and TLR4. The green residues are Ser28, Lys55, Lys128 and Gln155. (b) The comparison between the best dimer model of human (cyan) and mouse (orange)

Recall the recent experimental result that Taxol, a mitotic inhibitor used in cancer chemotherapy, functions as an agonist in mouse MD-2/TLR4, but as an antagonist in human MD-2/TLR4.[73] Then, the TLR4 dimerization or subsequent signaling in the mouse case can be interpreted as caused by Phe126 edge reshaping after Taxol binding. In other words, Taxol binding to mouse MD-2 causes reshaping of the 123-130 loop. It is directed outward from MD-2 so as to promote close approach to mouse TLR4, leading to TLR4 dimerization. However, in the human case, the presence of Taxol facilitates the formation of the concave surface at the Phe126 edge and blocks the subsequent signaling. In our protein-protein docking work, although no ligand binding is included in the

protein-protein docking, the mouse and human homodimers still reveal a difference in their binding strength: mouse binds tighter than human. If it represents the cellular situation, the contact surface would favor the mouse MD-2/TLR4 association and promotion of activation; an event predicted to be reinforced by the presence of Taxol.

## Chapter 4

### Lipopolysaccharide (LPS) binding to TLR4/MD-2 dimer

#### 4.1 Introduction

Lipopolysaccharide (LPS), a major constituent of the outer membrane of gram-negative bacteria, consists of polysaccharides and lipid structure named lipid A. [62] A small difference in LPS, has a great influence on host response against Gram-negative bacteria. [64] (i) Different number of acyl chains will lead to different response. Hexa-acylated lipid A stimulates the immune response, lipid IVa with four acyl chains was originally identified as an inhibitor of the human LPS receptor. (ii) The length and symmetry of the acyl chain also has a influence on host response. For example, both *Escherichia coli* lipid A and *Neisseria meningitidis* lipid A are hexa-acylated. However, the length and the symmetry of these six acyl chains in the two lipid A structures are not the same. **(Figure 4.1)** The recent experiment from our collaborator showed that meningococcal lipid A

with asymmetrical acyl chain distribution, similar to *E. coli* lipid A, showed increased biological activity when compared with a symmetrical acyl distribution (*Neisseria meningitidis* lipid A). Furthermore, KDO moiety is crucial for meningococcal LOS bioactivity since lipid A alone is not active and one KDO linked to that lipid A rescue the bioactivity.

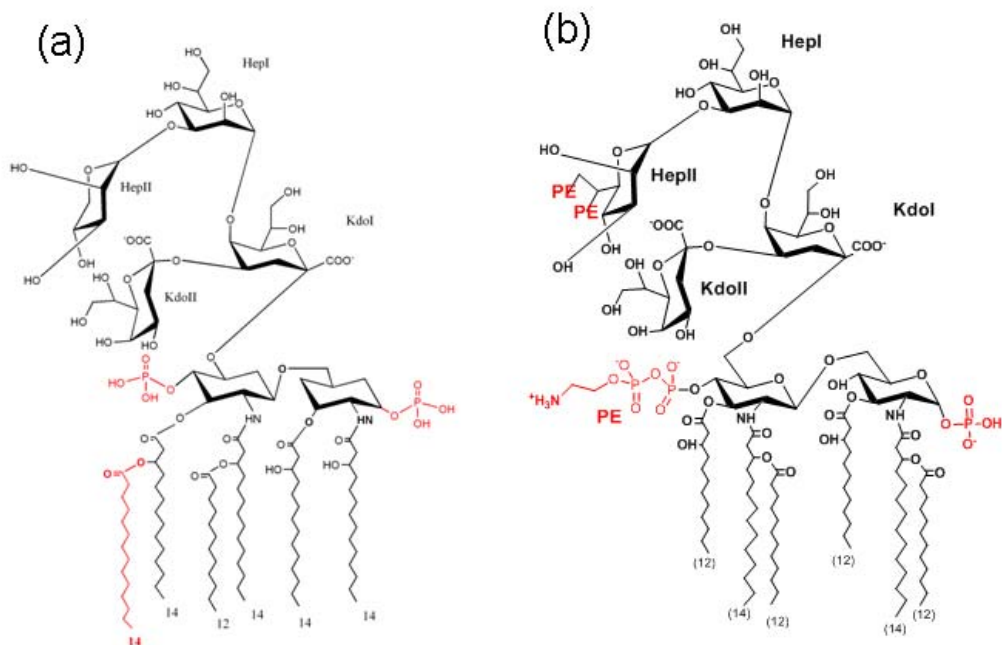


**Figure 4.1** (a) 2D structure of *E. coli* lipid A; (b) 2D structure of *Neisseria meningitidis* lipid A. One PEA group was added at 1-PO4 site.

## 4.2 Computational Methods

The crystal structure of TLR4-MD2-dimer complexed with Ra *E. coli* LPS (PDB code: 3FXI) was recently released.[74] Based on this crystal structure, Meningococcal LOS was docked into human TLR4/MD-2 dimer by Autodock 4.0. [75] Because the ligand Meningococcal LOS has large numbers of rotatable bonds, it is hard to dock this ligand with all rotatable bond setting to be flexible. Here, we tried to make four chains which are buried in the human MD-2 cavity to be rigid, while the other two chains (R2 and R2') which locate near the TLR4/MD-2 interface are flexible. The AutoGrid calculation was run with 70 points (separated by 0.503 Å) in each spatial dimension. AutoDock was run using the Lamarckian genetic algorithm, producing 50 structures, which were evaluated in the analysis step. Once all the docking steps are finished, the MM-GBSA scores for each docking poses are estimated by performing the Prime MMGBSA.

## 4.3 Results and Discussion

### 4.3.1 KDO group effect

For the Meningococcal LPS without KDO, we tried to dock this ligand into human TLR4/MD-2 dimer with different flexibility setting: whole ligand are rigid; one chain is flexible, other parts are rigid; and two chains are flexible, other parts are rigid. All docking poses are estimated based on their MMGBSA score. In this

case, docking pose with the whole Meningococcal LPS rigid has the best MMGBSA score -74.4 kcal/mol. In this docking pose, R2 acyl chain was exposed on the surface of MD-2, forming a hydrophobic core of interaction with Phe440 and Leu444 from TLR4\*. R2' chain is still buried inside the human MD-2 cavity. The KDO group forms Hydrogen bond with Tyr296 from TLR4, and the electrostatic interaction is formed between 4-PO4 and Arg264. (**Figure 4.2**)

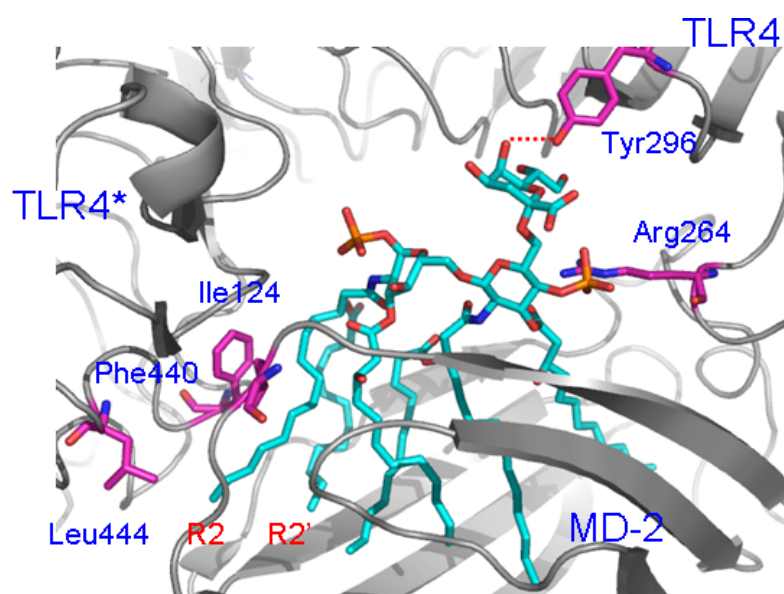


**Figure 4.2:** The best docking pose of Meningococcal LPS without KDO

For the Meningococcal LPS with KDO group, we also docked this ligand into human TLR4/MD-2 dimer three times with the similar flexibility settings as LPS without KDO. However, in these three flexibility settings, KDO group is always to set to be flexible. After the Prime MM-GBSA score calculation, the docking pose with two chains and KDO to be flexible has the best MMGBSA score -90.4 kcal/mol, which has 16 kcal/mol energy difference compared with

no-KDO docking result. In this docking pose, four acyl chains which are set to be rigid are still binding into the human MD-2 pocket. However, the other two chains are binding into the cavity which are formed by the human TLR4/MD-2/TLR4\* interface. R2 chain formed hydrophobic interaction with Val411 and Lys388 from TLR4\*, while R2' chain formed hydrophobic interaction with Phe408 and Arg382 from TLR4. (**Figure 4.3**)

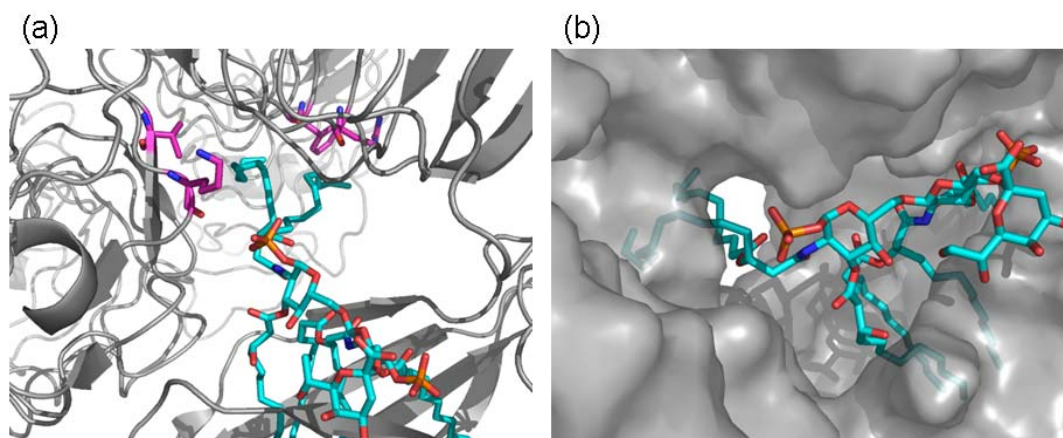


**Figure 4.3:** (a) The best docking pose of Meningococcal LPS with KDO. (b) The best docking pose of Meningococcal LPS with KDO; the receptor is shown in surface view (grey).

Recently, Park et. al. compared the E.coli LPS and TLR4/MD-2 antagonists eritoran and lipid IVa after superimposition of MD-2. In this comparison, the glucosamine backbone of E.coli LPS has a  $\sim 5\text{\AA}$  shift upwards in both cases. This shift may provide additional space for R2 and R2' binding and make PO<sub>4</sub> group to get close to positively charge residue on TLR4 protein.[76] This comparison

---

indicates that this shift is important because MD-2 cavity is not big enough to contain all six acyl chains of lipid A, and additional space for lipid binding is generated by this shift. **(Figure 4.4)** Here, we compared the Meningococcal LPS binding with or without KDO by superposing the TLR4/MD-2 receptor, the glucosamine backbone of Meningococcal LPS with KDO also had a 3.7Å shift upwards compared with LPS without KDO, which indicated that Meningococcal LPS with KDO may have more broad space for the acyl chain binding and link the TLR/MD-2 dimer more tightly than LPS without KDO. **(Figure 4.5)** The docking results showed that Meningococcal LPS with KDO binding has lower energy score than LPS without KDO binding, and also LPS with KDO has a 3.7Å shift upwards compared with LPS without KDO. It indicated that LPS with KDO performed better than LPS without KDO which is consistent with the experiment result that lipid A alone is not active and one KDO linked to that lipid A rescue the bioactivity.

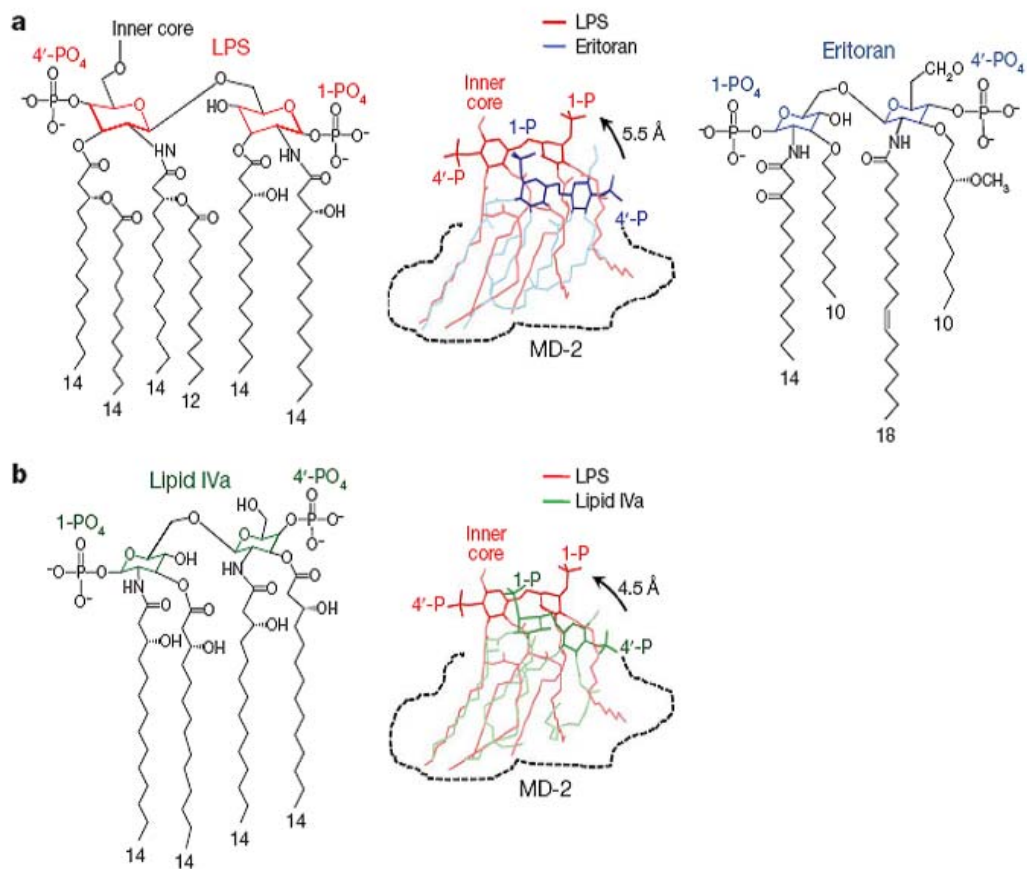


**Figure 4.4 (a)** Comparison of E.coli LPS and Eritoran after superimposition of MD-2. LPS and Eritoran are color red and blue, respectively. **(b)** Comparison of E.coli LPS and lipid IVa. The structures of LPS and lipid IVa are shown after superimposition of MD-2. The shape of the MD-2 pocket is drawn schematically with broken lines. The glucosamine rings and the phosphate groups are represented in darker color.

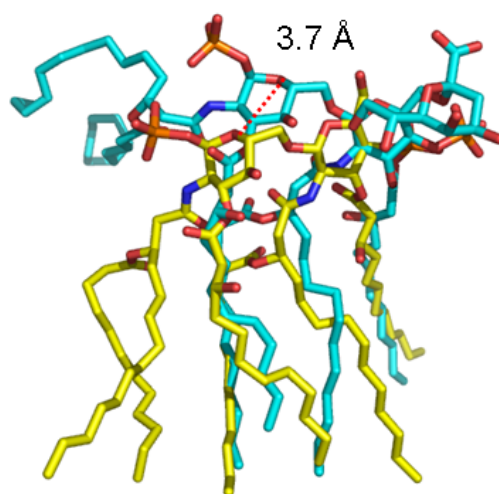


**Figure 4.5** Comparison of LPS with KDO (blue) and LPS without KDO (yellow) after superimposition of MD-2

#### 4.3.2 PEA group adding to LPS

Meningococcal LOS is hyper phosphorylated and biologically very active. We could add two phosphate groups on 1 position or 4' position with PEA, and this PEA group is setting to be flexible during docking. For PEA group adding to 1-PO4 site, the MM-GBSA score for besting pose is -81.2 kcal/mol. In this pose, KDO group will form hydrogen bond with Lys341 on TLR4. Electrostatic interactions are formed between 4-PO4 and Arg264 with 2.7 Å N $\cdots$ O distance, and between 1-PO4-NH $_3^+$  and Asp395 with 2.8 Å N $\cdots$ O distance. There is a 0.7 Å displacement to TLR4\* side comparing with M.LPS rigid docking pose.

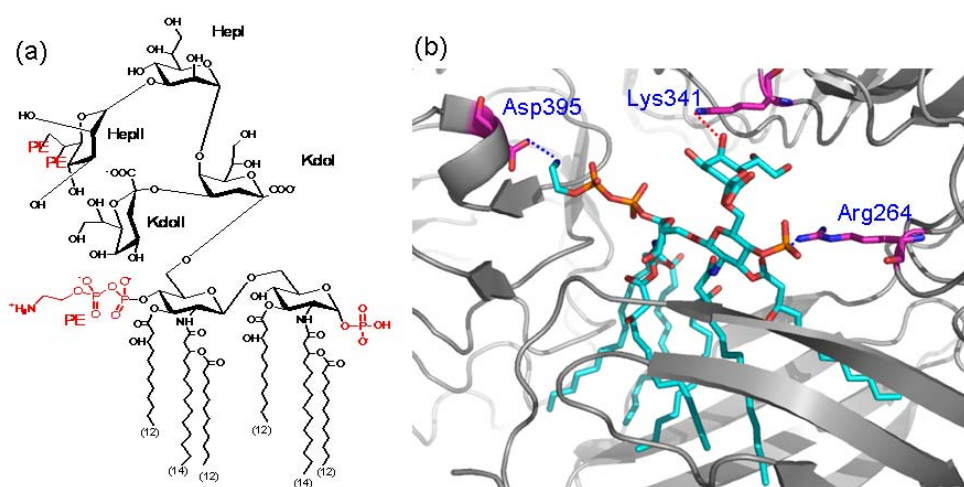


**Figure 4.6** (a) 2D structure of Meningococcal LPS with one PEA group added at 1-PO4 site. (b) The docking pose of Meningococcal LPS with one PEA group at 1-PO4 site.

For PEA group adding to 4-PO4 site, the MM-GBSA score for besting pose is -84.8 kcal/mol. In this pose, KDO group will form hydrogen bond with Tyr296 on TLR4, and another hydrogen bond was formed between 1-PO4 and Ser415. Electrostatic interactions were existed between 4-PO4 and Arg264 with 2.7 Å N $\cdots$ O distance, and between 4-PO4-NH $_3^+$  and Asp294 with 3.1 Å N $\cdots$ O distance. There is a 0.8 Å displacement to TLR4 side comparing with M.LPS rigid docking pose. (**Figure 4.7**)

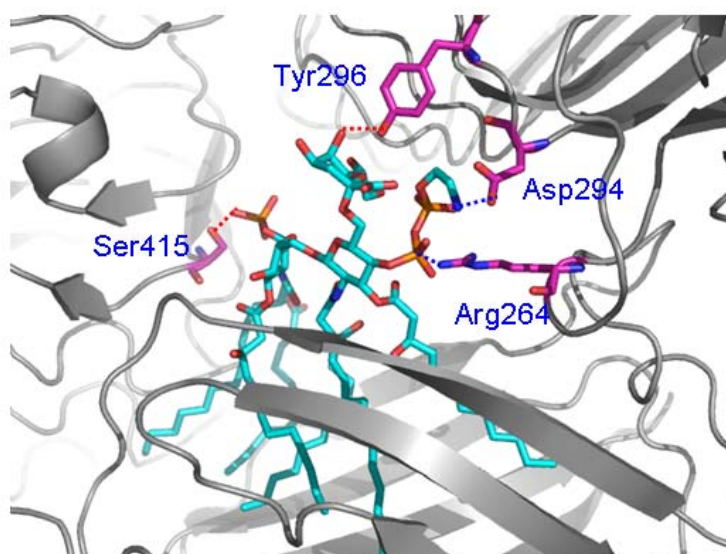


**Figure 4.7** The docking pose of Meningococcal LPS with one PEA group at 4-PO4 site.

We also add two PEA group at each PO4 site, and the MM-GBSA score for besting pose is -98.2 kcal/mol. In this pose, electrostatic interactions are formed between 1-PO4-NH3<sup>+</sup> and Asp395 with 2.8 Å N···O distance, between 4-PO4 and Arg264 with 2.7 Å N···O distance, and between 4-PO4-NH3<sup>+</sup> and Asp294 with 3.1 Å N···O distance. (**Figure 4.8**)

The docking scores and the details of these docking pose indicate that adding of PEA group will provide extra electrostatic interactions with positively and negatively charged residues on TLR4 and TLR4\* proteins which will lowered the MM-GBSA score and lead to tightly binding.

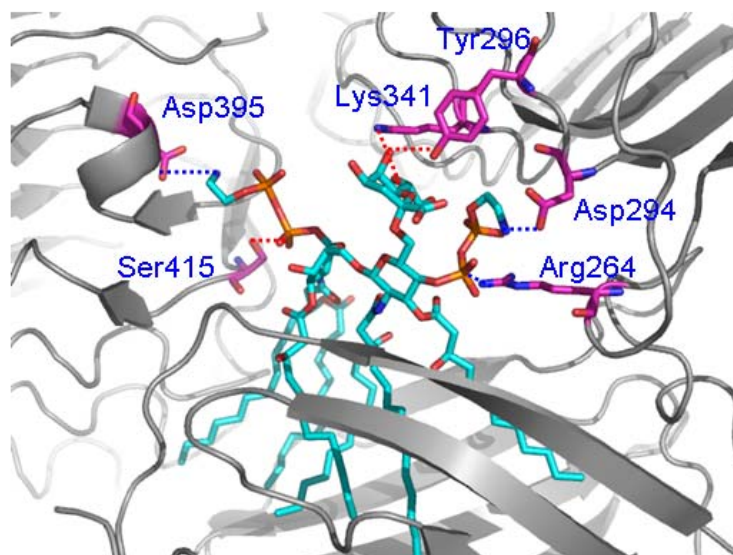


**Figure 4.8** The docking pose of Meningococcal LPS with two PEA groups at each PO4 site.

## Chapter 5

### Density Functional Calculation of Cross-Coupling Reaction between series of Gilman Cuprates and CH<sub>3</sub>I

#### 5.1 Introduction

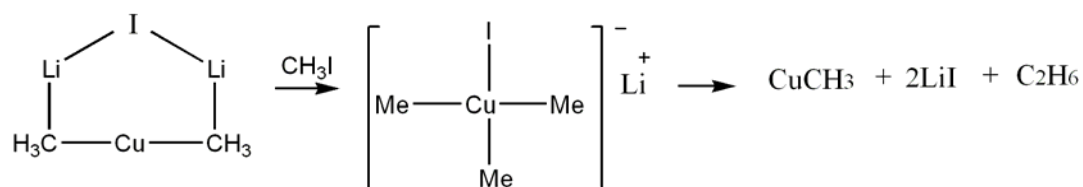
Organocuprate, facilitating the selective creation of carbon-carbon bonds, is an important synthetic methodology. Two typical reactions of organocuprates include conjugate addition to  $\alpha$ ,  $\beta$  unsaturated carbonyl compound and S<sub>N</sub>2-like substitution reaction of alkyl halides (cross-coupling with organic halides).[77] The intermediate in such copper-mediated cross-coupling reaction has long been believed to be the “copper (III) intermediate”, which is a tetracoordinate, square-planar (TCSP) complex. [78] In 2007, Bertz *et. al.* applied the low temperature rapid injection NMR (RI-NMR) to investigate the reactions of methyl Gilman reagents, Me<sub>2</sub>CuLi·LiX (X=I, CN, SCN, SPh), with EtI, and

observed stable TCSP intermediates.[79] However, the mechanism for this cross-coupling reaction is still unclear. We have performed the ab initio calculation to propose reasonable mechanism in the cross-coupling reaction, involving  $\text{Me}_2\text{CuLi}\cdot\text{LiX}$  ( $\text{X}=\text{I}, \text{SCH}_3, \text{CN}$ ) and  $\text{CH}_3\text{I}$  reagents.

## 5.2 Results and Discussion

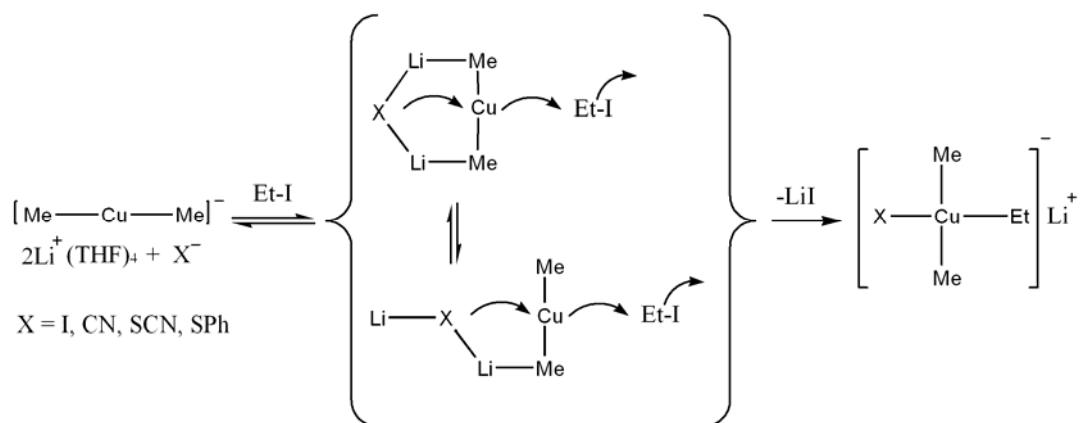
The theoretical lowest energy isomer for solvated  $\text{Me}_2\text{CuLi}\cdot\text{LiCN}\cdot(\text{H}_2\text{O})_2$  has been applied to Gilman cuprate  $\text{Me}_2\text{CuLi}\cdot\text{LiX}$ . The resulting structure is best described by a lower-order dimethylcuprate anion bridged by the  $\text{Li}_2\text{X}$  cation. [80] The systematic study showed that B3LYP method with the basis set incorporating the relativistic effective core potential for Cu and the 6-31G\* basis set for the rest is the most cost-effective theoretical method for the studies of the structure and energetics of organocuprate species, therefore, we performed the calculation at the level of B3LYP/LANL2DZ, 6-31G\*. [81]

For copper-mediated cross-coupling reaction,



Bertz, et. al. proposed a symmetrical mechanism for the formation of TCSP intermediates: Et-I reagent with the cuprate complex keeps the  $\text{C}_s$  symmetry;

ethyl group connected to the copper in the symmetrical way, while iodine atom went away.



Scheme 1: Proposed mechanism for the formation of TCSP intermediates[79]

However, our calculation demonstrated that  $\text{CH}_3\text{I}$  prefers to attack Gilman cuprate in an asymmetric way. The geometry of the first transition state showed that  $\text{CH}_3\text{I}$  reagent is on top of the Gilman cuprate plane, with the 2.21 Å distance from  $-\text{CH}_3$  to Cu, and the 2.82 Å distance from I to Li, suggesting that  $\text{CH}_3\text{I}$  attacks the cuprate group from the upside. The iodine group in  $\text{CH}_3\text{I}$  attracts one of the lithium in Gilman cuprate to trigger a tiny violation to the cuprate plane, emphasizing the importance of the lithium.

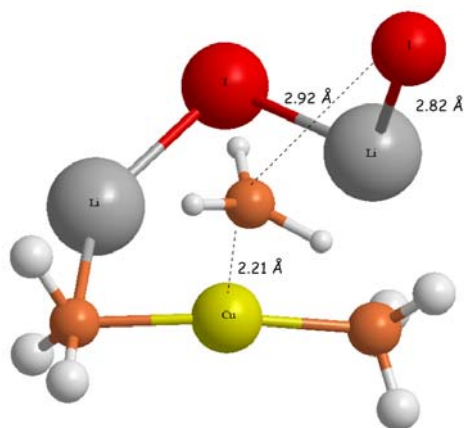


**Figure 5.1:** The first transition state of cross coupling reaction. (Grey: Li; Red: I; Yellow: Cu; Orange: C; White: H)

The intermediate in this calculation was nearly a tetracoordinate, square-planar complex, which is consistent with the experiment result. However, two lithium atoms were on the left side of this symmetrical TCSP complex, which promoted the middle methyl group approaching to another methyl on the right side to form a new carbon-carbon bond.

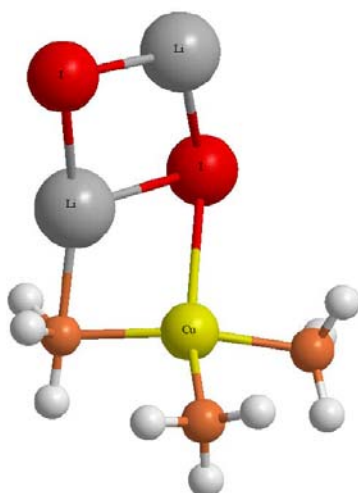


**Figure 5.2:** The intermediate of the cross coupling reaction

The schematic potential energy surface for this reaction is shown in Figure 3. One pre-reactive complex was found to be 5.28 kcal/mol energies lower than reactant. The energy barrier is 28.98 kcal/mol for the first transition state. One interesting feature is that the second transition state has a very low energy barrier, only 0.3kcal/mol, resulting in a quite unstable state.

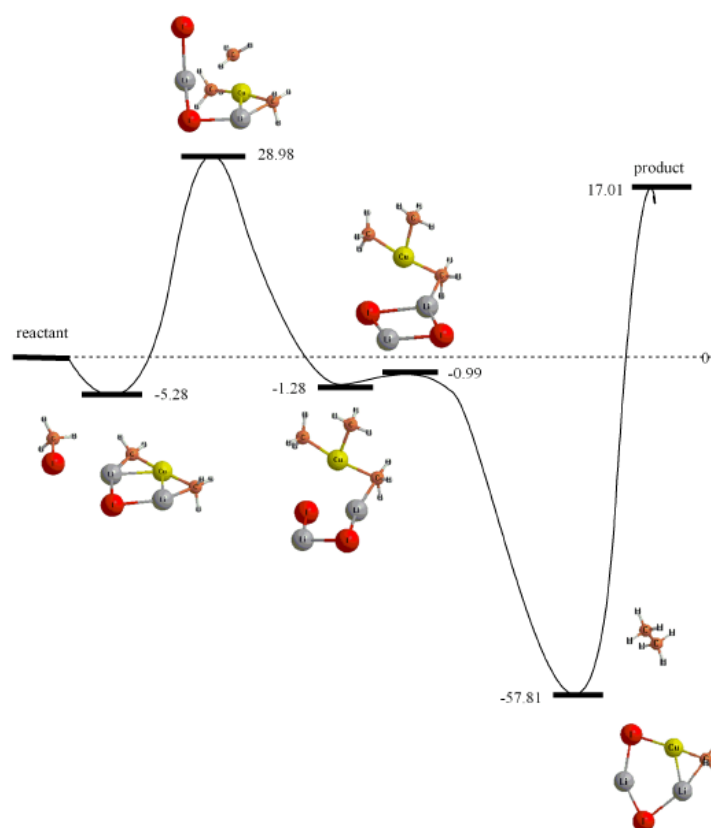


**Figure5.3:** The schematic potential energy surface for the cross-coupling reaction

The calculation, which was also performed on  $\text{Me}_2\text{CuLi}\cdot\text{LiX}$  ( $\text{X}=\text{CN}$ ,  $\text{SCH}_3$ ), showed the quite similar result for the mechanisms.  $\text{CH}_3\text{I}$  reagent attacks the

cuprate group in an asymmetric way, further confirmed the asymmetric mechanism we proposed. The intermediates for these two are TCSP complexes, similar to the iodine case.

From the ab initio calculation, we confirmed that the intermediate for copper-mediated cross-coupling reaction is a tetracoordinate square-planar complex. The first transition state implied a new asymmetric pathway in this cross-coupling reaction. The importance of the lithium was emphasized.

## Chapter 6

### Structure-based design and synthesis of inhibitors of histone lysine methyltransferase (H3K9me2)

#### 6.1 Introduction

Histone lysine methylation plays a key epigenetic role in the regulation of chromatin and gene expression.[82] This can be mediated by more than 50 (SET-domain) histone lysine methyltransferase (HKMTase) enzymes that are present in the mammalian genome. HKMTase enzymes differ in their specificity for target lysine residue in inducing mono-, di-, or trimethylation. For instance, enzymes such as G9a and G9a-like protein (GLP) are known to induce mono- and dimethylations, where as enzyme Suv39h known to catalyze trimethylation. Studies suggest that these HKMTase enzymes are implicated in tumor development. For example, repressive methylation states on H3K9

---

(histone3-lysine9) and H3K29 (histone3-lysine29) are detected at promoter regions of aberrantly silenced tumor suppressor genes in cancer cells; siRNA knockdown of G9a, GLP resulted in upregulation of E-cadherin in cancer cells where this gene was epigenetically downregulated. Down regulation of E-cadherin is a hallmark of the epithelial-mesenchymal transition that underlies the progression of cancer to metastasis.[83] Moreover G9a has been implicated in the function of CutL1.[84] CutL1 is a transcription factor that activates a transcriptional program regulating genes involved in cell motility, invasion, and extracellular matrix composition downstream of TGFbeta signaling.[85] Chemical inhibitors of G9a could thus potentially contribute to upregulation of E-cadherin and attenuation of CutL1 function with the hopes of impeding the shift to metastasis.

Many other HKMTases are also promising targets for discovery of small-molecules. For example, EZH2, a histone H3K27 HKMT overexpressed in many aggressive cancers.[86] Inhibition of EZH2 by siRNA has been shown to prevent metastasis of PC-3 prostate cancer cells in mice.[87] Moreover, there is accumulating evidence to implicate HKMTases such as Smyd3, SETDB1, NSD1, NSD2, NSD3, and Suv39h1 in human cancers.[88, 89] Taken together, the current data convince that many of these HMTases very important and potentially druggable targets for various types of cancer.

As per as the discovery of the small molecule inhibitors to these HKMTases are concerned, very limited efforts have been appeared in the literature.[90, 91]

---

But recently Kubicek et al., have identified an interesting compound **1** (BIX01294) as an inhibitor of the G9a HMTase, by high-throughput screening method from the 125,000 compound library.[92, 93] In their study, this analog was found to show low micromolar activity ( $IC_{50} = 2.7 \mu M$ ) and selective activity to G9a enzyme (a dimethylating enzyme) over other HMTases Suv39h1 (a trimethylating enzyme) and PRMT1 (arginine methyl transferase enzyme). Moreover, this compound was used by others to reprogram the mammalian somatic cells into induced pluripotent stem (iPS) cells, and to generate iPS cells from mouse fetal neural precursor cells.[93, 94] Inspired by the promising biological results presented by this analog, we recently interested and investigated the structural basis for the inhibition of G9a enzyme by this molecule.[95] In our earlier report, we have shown that this analog binds to G9a enzyme at acidic binding groove and then it prevents the peptide substrate binding. We also solved the X-ray structure (at 2.7 Å) of G9a enzyme SET domain in complex with BIX01294 ligand **1**. Although analog **1** has proven to be good inhibitor of G9a and G9b enzymes in our hand, its activities were still in the sub-micromolar level. It would be prudent to have molecule with low nanomolar activities for in vivo biological investigations.

## 6.2 Structure-based Modeling of GLP Ligands

### 6.2.1 Computational Methods

Efforts to improve the potency of **1** employed the X-ray structure of the GLP/BIX-01294 complex as a template for structure-based design. Both the protein structure and preliminary docking models suggested three sectors of the ligand as best suited for structural modifications: a) the diazepine ring, b) the piperidine ring benzyl appendage, and c) the C7-methoxy groups (**Figure 6.1**).

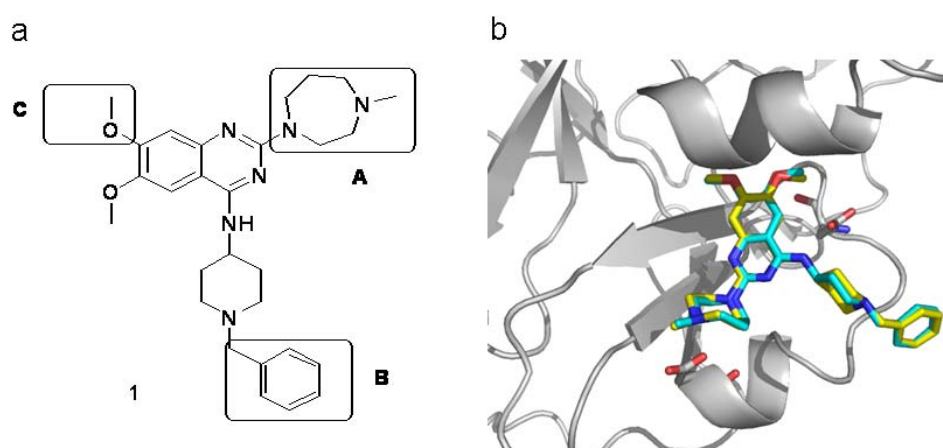


**Figure 6.1.** BIX-01294 centers for structural modification (left); X-ray (yellow) and Glide (cyan) docking poses of the ligand in the GLP binding site.

All designed analogs were docked flexibly into GLP (G9a like protein) (PDB code: 3FPD)[95] with extra precision Glide (Schrödinger, LLC). This methodology regards the protein structure as a rigid body, but treats the ligand as

---

a conformationally flexible molecule. The resulting GLP/analog complexes were subsequently sorted energetically with the MMGBSA scoring algorithm, which provides an estimate of relative binding free energies. As a test of this approach, BIX-01294 was Glide-docked into the X-ray structure of GLP/BIX-01294 depleted of ligand. While a number of different binding poses resulted, the MMGBSA energy sorting selected a pose that is virtually identical to the X-ray structure as the best match (**Figure 6.1**). In fact, this same pose resulted from the docking exercise during the refinement of the protein-ligand complex prior to final fitting of ligand and ligand-density.[95]

### **6.2.2 Structure-based Prediction of BIX-Analog Binding Poses.**

For modifications at Site A of BIX-01294 (**Figure 6.1** and **6.2a**), the diazepine ring was replaced with several moieties to examine the effect of positively charged groups as complements to the oppositely charged binding site residues Glu and Asp. Each of the analogs was Glide-docked into the binding site of the protein with a maximum of 30 distinct poses scored by Glide, all of which were energetically rescored with the MM-GBSA scoring function as tabulated in **Figure 6.2c**. The acyclic amine class (n = 2-5) was predicted to display reasonable binding affinities, with MM-GBSA scores of -32.0 to -37.0 kcal/mol. For 2-carbon diamine analog, this substitute doesn't mimic the diazepine ring, and H-bond with Asp1131 is lost. For acyclic amine (n=3) analog, **6a** although the 3-carbon diamine chain mimics the conformation of the diazepine

---

ring, one carbon missing will lead to losing some hydrophobic interactions with Cys1155. If we compare **6a** with BIX-01294, we overlapped the molecular surfaces of this analog with BIX-01294, and they overlapped quite well. The difference between these two molecules is the flexibility. It seems that 3-carbon diamine analog is more flexible than BIX-01294. For 4-carbon diamine analog, this substitute mimics the diazepine ring in reverse direction and loses the H-bond with Asp1131. For 5-carbon diamine analog, this 5-carbon chain is too bulky to fit into this cavity. Many bad contacts are created by the binding. Of particular interest, the N,N-dimethyl-aminopropyl analog **6a** was forecast to possess a binding orientation nearly identical to that of BIX-01294. The three-carbon diamine chain mimics the conformation of the diazepine ring and, like the X-ray structure and docking model of BIX-01294 (**Figure 6.1**), engages in two hydrogen-bonds with Asp1131 and Asp1140 (**Figure 6.2b**). The mass spectrometry-based GLP enzyme inhibition assay for this compound reported submicromolar methylation activity to be essentially the same as that for BIX-01294 (IC<sub>50</sub> values of 0.8 and 0.7 μM, respectively).

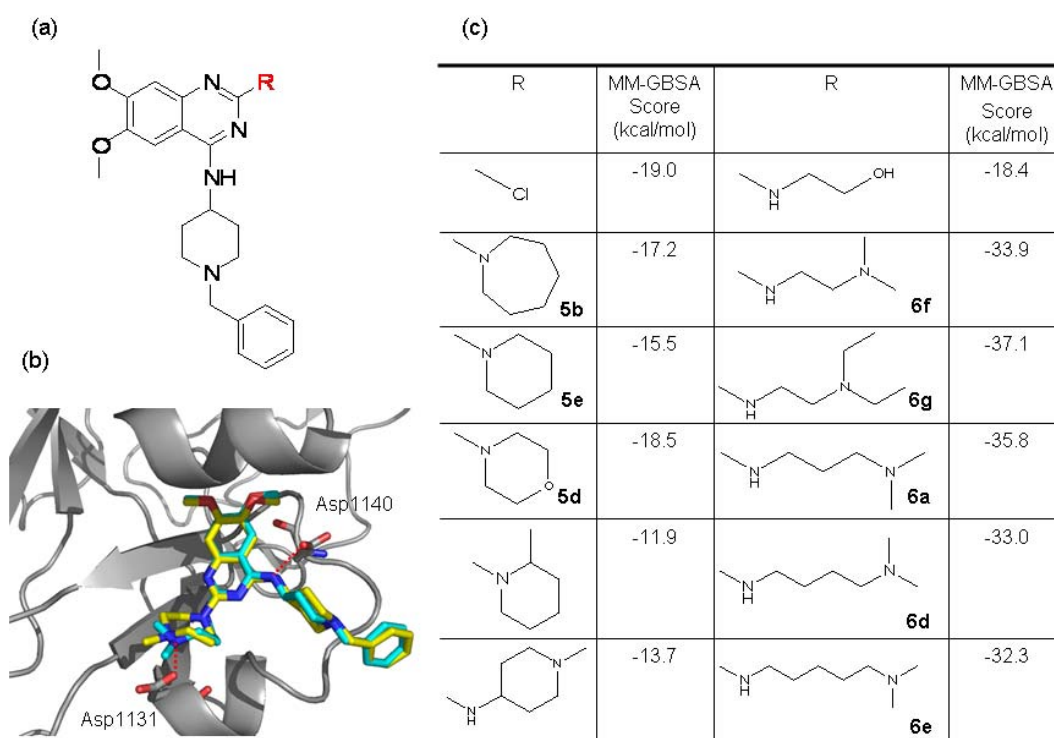


**Figure 6.2** (a) Site A region in BIX-01294 can be populated by different groups; (b) Best docking pose for the N,N-dimethyl-aminopropyl chain in the site A region (cyan) superimposed with the X-ray structure of BIX-01294 (yellow). (c) Substituents at site A and best-pose MM-GBSA scores.

The primary Site B modification (**Figure 6.1**) eliminated the solvent-exposed hydrophobic benzyl group on the piperidine ring. The corresponding MM-GBSA score of -37.0 kcal/mol is 5 kcal/mol less favorable than that for the original BIX-01294 inhibitor (-42.0 kcal/mol). The predicted binding orientation for this analog mimics the BIX-01294 X-ray structure closely. It also forms two H-bonds

with Asp1131 and Asp1140. (**Figure 6.3**) However, reduction of the methylation activity for this benzyl-truncated analog is approximately 5-fold less than that exhibited by BIX-01294. Although exposure of the benzyl group to solvent might be regarded intuitively as a detriment, the binding site molecular surfaces for GLP and BIX-01294 show a satisfying complementary fit for the N-benzyl moiety (See the Supporting Information). Thus, hydrophobic collapse of the latter with the GLP loop around Ala1138 would seem to more than compensate for the inhibitor's phenyl ring residing partly in the water layer.

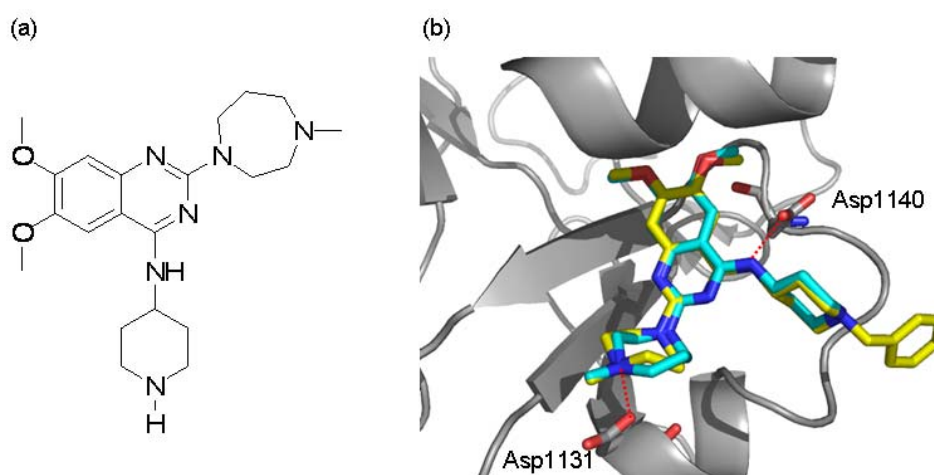


**Figure 6.3** (a) BIX analog in which the benzyl moiety has been eliminated; (b) Best docking pose of the benzyl-depleted analog (cyan) superimposed with BIX-01294 in the GLP protein.

Site C modifications (**Figure 6.1**) extended the C7-methoxy group of

BIX-01294 into two channels of the protein that diverge near the subsite in which the C7 group resides. Channel 1 is the substrate lysine-binding groove directed toward the cofactor AdoHcy (S-adenosyl-homocysteine). The other is Channel 2 that flows toward the solvent. (**Figure 6.4**) To explore occupation of the channels, in the first instance a protonated amine was added at the end of the C7 chain to generate  $(\text{CH}_2)_n\text{N}^+\text{H}_3$  ( $n = 1-7$ ). For **18c** ( $n = 4$ ) the cationic head binds within the lysine-binding channel and forms a hydrogen bond with Tyr1124, a residue close to the cofactor. The MM-GBSA scores for this modification (**Figure 6.5**) were significantly improved ( $\Delta\Delta G = 21$  kcal/mol) by comparison with BIX-01294. These results are in satisfying agreement with the measured  $\text{IC}_{50}$  values of  $\sim 0.3$  and  $\sim 0.1$   $\mu\text{M}$  for **19b** ( $n = 5$ , **Figure 6.5**) and **21a**, respectively.

Glide docking of **21a** into the binding site of GLP is depicted in **Figure 6.6**. The core of the molecule is predicted to bind with an  $0.6 \text{ \AA}$  shift relative to BIX-01294, while the C7O substituent resides in Channel 1 as pictured for **18c** in **Figure 6.5**. The shift contributes to the H-bond formed from Asp1145 to the exocyclic NH for both **19b** and **21a** as represented in **Figure 6.6**. Finally, an important binding element predicted by docking arises from replacement of the N-benzyl group with a  $(\text{CH}_2)_5\text{NH}_3^+$  chain that folds back on the protein to make a salt bridge with Asp1135.

Alternatively, when structures that incorporate long hydrophobic chains from the C7-oxygen ( e.g.  $(\text{CH}_2)_n\text{CH}_3$  or  $(\text{CH}_2)_n\text{Ph}$  ( $n = 0-7$ )) were docked into the

---

binding pocket, they prefer Channel 2. The corresponding MM-GBSA scores improved by up to 4 kcal/mol relative to BIX-01294, presumably as a result of the increase in surface area shared by ligand and protein. (**Figure 6.7**) This is consistent with the presence of several Phe residues and a Pro at the entrance of Channel 2 causing it to be more hydrophobic than Channel 1.

These channel-populating ligand enhancements increase the molecular weights of the modeled analogs to values above 500. This suggests that the length of the more extended chains with superior MM-GBSA binding scores is probably less than ideal. While the calculated MM-GBSA for shorter chains decrease slightly, they nonetheless imply that the lower molecular weight analogs may still be better ligands than BIX-01294 itself in a cellular environment. **Figures 6.8** and **6.9** reveal that with decreasing length of the carbon chain from C7-O, the MM-GBSA scores diminish simultaneously. Nonetheless, the predicted binding affinities of the shorter chains are still superior to that calculated for BIX-01294 (-42 kcal/mol).

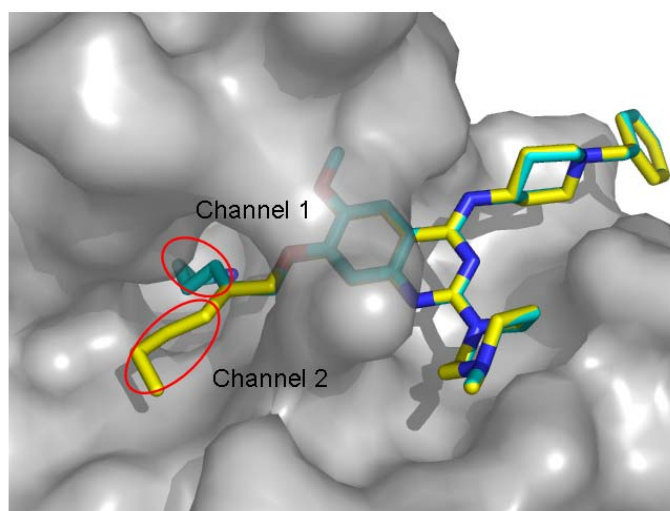


**Figure 6.4** C7-OMe substitution can branch into two channels. The more polar Channel 1 follows a path to the cofactor AdoHcy, while the more hydrophobic Channel 2 is directed toward the solvent.

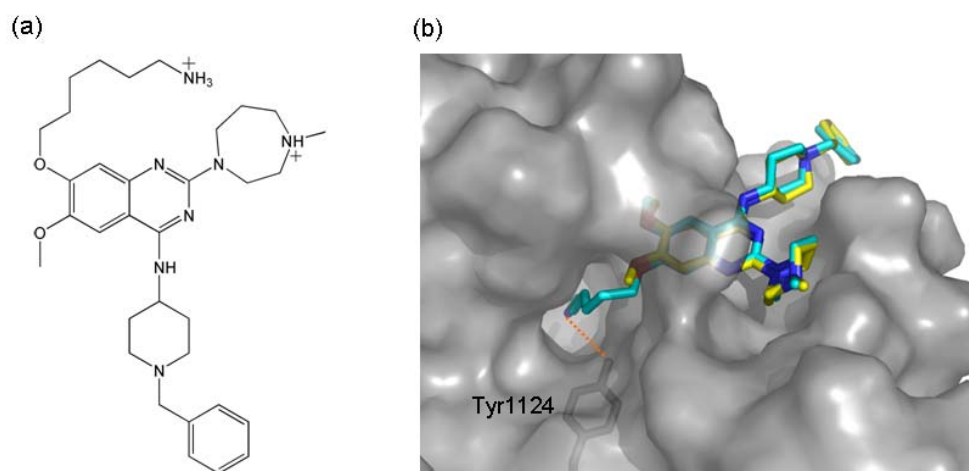


**Figure 6.5** The protonated dimethylamine coupled to C7-OMe by an  $n = 6$  carbon chain, **18c** (a) in its best docking pose within the GLP protein (b).

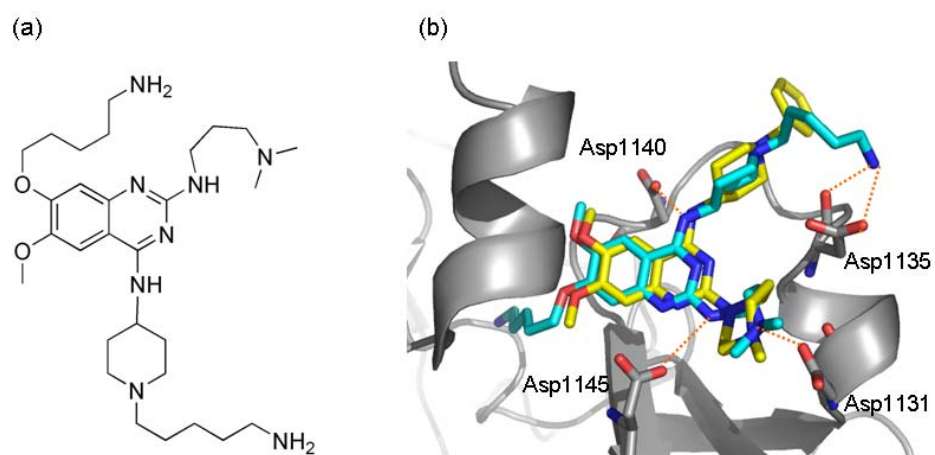


**Figure 6.6** The 2D structure of **21a** (a) and its Glide-determined docking pose in GLP (b).

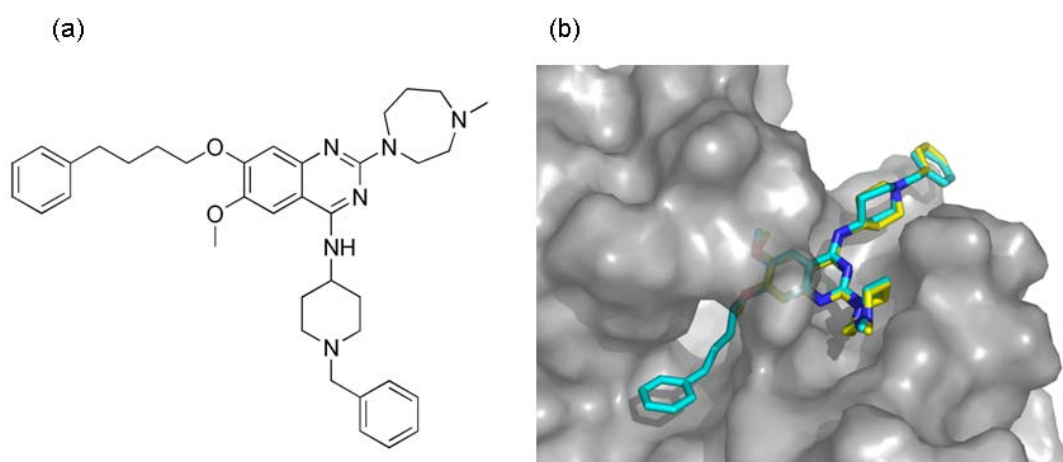


**Figure 6.7** An extended hydrophobic substituent coupled to C7-OMe, **13b**, (a) in its best docking pose within the GLP protein (b).

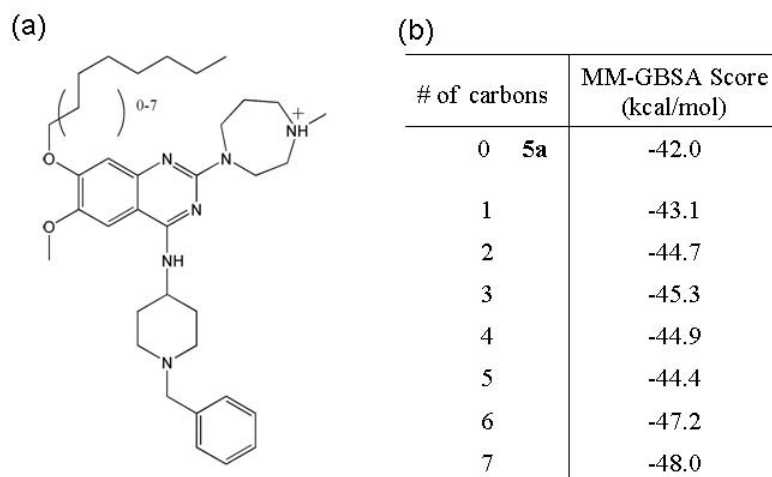


**Figure 6.8** Increasing the number carbons from C7O that carry the terminal protonated amine causes a corresponding increase in predicted binding energy (MM-GBSA score) between the docked ligand and GLP.

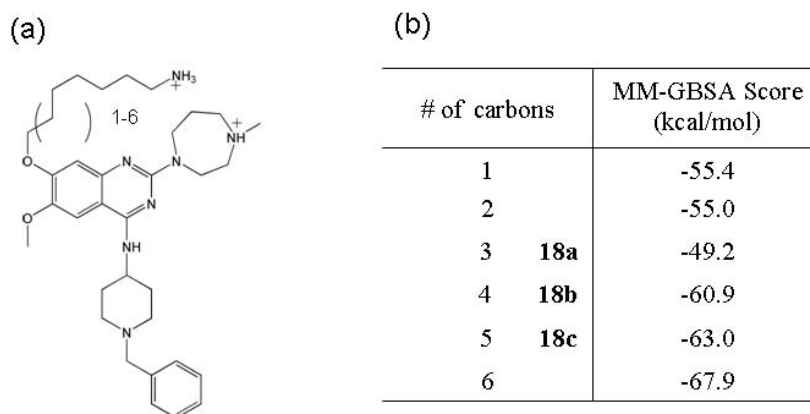


**Figure 6.9** Increasing the number carbons from C7O that carry a hydrophobic chain causes a corresponding increase in predicted binding energy (MM-GBSA score) between the docked ligand and GLP. The value of  $n = 0$  corresponds to

BIX-01294.

### 6.3 Conclusion

Histone lysine methyltransferases are emerging as promising targets for understanding epigenetic control of hetero-chromatin-mediated gene expression and, ultimately, therapeutic intervention. Effective and selective HKMT inhibitors would contribute immeasurably to both phenomena. The recently reported BIX-01294 is a promising inhibitor of the G9a and GLP H3K4 enzymes, although its potency is probably insufficient for in vivo biological studies. As a first step to remedying the situation, our group recently solved the X-ray structure of the GLP/BIX-01294 complex. In the present work, we employed the latter structure, intuitive analysis and molecular modeling to conceive a family of analogs and to predict that a subset would be more potent histone methyltransferase blockers than the parent, BIX-01294. Subsequent synthesis and biological testing identified a number of analogs with activity equivalent to the latter. However, two of the analogs, **6e** and **21a**, proved to be 5-10 fold more potent than the original compound. These activities are in complete accord with the X-Ray and docking predictions.

## Chapter 7

# Benzenesulfonamides as a New Class of Chemokine Receptor Type 4 Inhibitors

### 7.1 Introduction

G-protein coupled receptor (GPCR) CXCR4 and the chemokine stromal cell-derived factor-1 (SDF-1/CXCL12) play a crucial role in physiological processes such as leukocyte migration/trafficking and hematopoiesis.[96, 97] The interaction of SDF-1 with CXCR4 has implications in cancer metastasis[98-100] and CXCR4 is a co-receptor for HIV-type1 infection.[101-103] CXCR4 has also been shown to be overexpressed in solid tumors as compared with normal tissue. Activation of the CXCL12 pathway can lead to recruitment of distal stroma by tumor cells to facilitate tumor growth and metastasis, as well as promote angiogenesis, cancer cell survival and invasion. Therefore, disruption of the

interaction of SDF-1 with CXCR4 can potentially block or delay metastasis.

Thus far, the most explored non-peptidic anti- CXCR4 agents are bicyclams such as AMD3100 and its derivatives.[104] However, their metal chelating properties leads to cardiotoxicity and therefore limit the use of these compounds.[104] Recently, we also indentified a novel class of CXCR4 antagonists [105], that led to a potent compound - WZ119 (**Figure 7.1**) and other dipyrimidine derivatives.[106] We are currently exploring other scaffolds that may lead to more potent and bioavailable compounds. Therefore, we designed and synthesized several benzenesulfonamide analogs. A competitive binding assay using the peptidic CXCR4 antagonist TN41003 was employed as a primary screening method for the new analogs.[105, 107] The compounds were further analyzed in a matrigel invasion assay and the *in vivo* effect studied in a paw edema for inflammation mouse model.

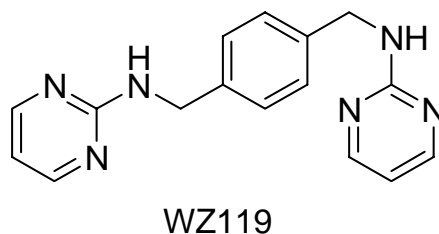


**Figure 7.1** 2D structure of WZ119

## 7.2 Results and Discussion

### 7.2.1 Structure-Activity Relationship (SAR) Study

We separately probed the regions to the left (Region A) and the right (Region B) of the benzenesulfonamide structural motif. That is, we varied  $R_1$  and  $R_2$ , as well as  $R_3$  and  $R_4$  to determine the effect on the activity of these compounds (**Figure 7.2**). These compounds were screened using the competitive binding assay with the CXCR4 antagonist TN41003 as previously described. Additionally, the matrigel invasion assay was used as the secondary functional assay to test whether they could block the CXCR4/CXCL12-mediated chemotaxis and invasion.

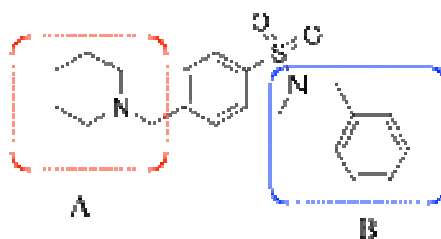


**Figure 7.2** Two regions (A and B) modified for structure-activity relationship study

Several cyclic and acyclic amines were introduced to region A of the benzenesulfonamide motif. Next, Region B was explored, retaining the piperidine, pyrrolidine and the diethylamine groups in region A, while adding various groups

in the para-position of the phenyl ring of region B. We then test the relative binding affinities of these analogs in CXCR4 receptor by using computational modeling methods.

### **7.2.2 Computational Protein-Ligand Docking**

The acid dissociation constant (**pKa**) of the benzene sulfonamide derivatives was predicted by ACD software.[108] Based on the pKa values, the protonation state of the nitrogen sites in these compounds was determined. All prepared benzene sulfonamide derivatives with the appropriate N-site protonated were docked flexibly into the cavity region of the human chemokine receptor CXCR4 crystallographic structure (PDB code: 3ODU) devoid of small-molecule antagonist IT1t using Glide with standard precision (Schrödinger, LLC).[109] This methodology regards the protein structure as a rigid body, but treats the ligand as a conformationally flexible molecule. The resulting CXCR4/benzenesulfonamide complexes were subsequently sorted energetically with the MM-GBSA scoring algorithm, which provides an estimate of relative binding free energies. The volume of the CXCR4 cavity was obtained by the web-based CASTp package.[47]

---

### 7.2.3 Mapping of the CXCR4 Antagonists Binding and SDF-1 N-terminus Binding

Compared with previous GPCR structures, the binding cavity of CXCR4 is larger and more open with 3322 Å<sup>3</sup> cavity volume. The small-molecule antagonist IT1t only occupies part of the pocket.[109] Several functional studies of mutant CXCR4 showed that Asp97, Asp187, Glu288, F87, D171 and F292 are required for SDF-1 binding, while the first three residue mutants impair SDF-1 signaling.[110, 111] The cyclic peptide TN14003 (T140) and CVX15 are CXCR4 antagonists of known structure. CXCR4 alanine scanning mutants identified that residues required for T140 binding are Asp171, Arg188, Tyr190, Gly207 and Asp262.[112] Recently, the crystallographic structure of CXCR4-CVX15 complex was released.[109] By combining the mutational analysis and the crystal structure, we can map the binding sites of the CXCR4 antagonists and the SDF-1 N-terminus. Mapping the T140 and CVX15 mutants onto the CXCR4 structure showed that these two peptide antagonists occupy similar sectors of the CXCR4 binding cavity, (**Figures 7.3b-c**) since most of the key residues for T140 binding are in close contact with CVX15. However, the SDF-1 N-terminus binds in another sector of the binding pocket, (**Figure 7.3a**) and a small overlap between peptide antagonist binding and SDF-1 N-terminus binding exists. (**Figure 7.3d**)

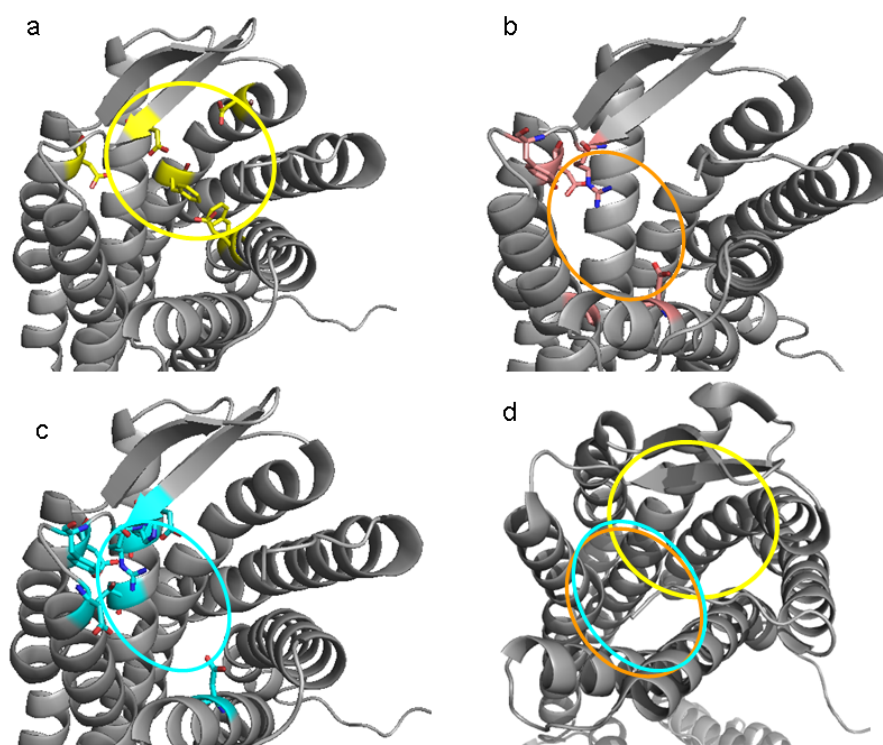
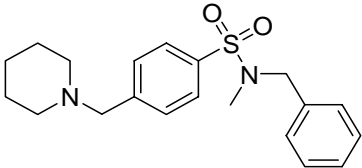
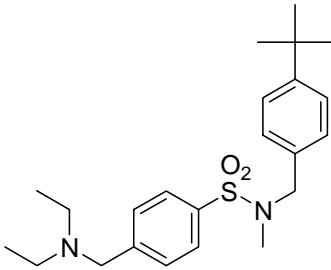


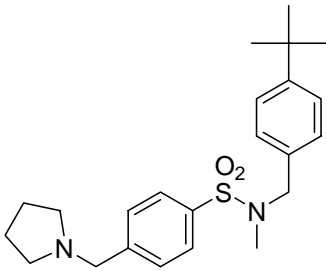
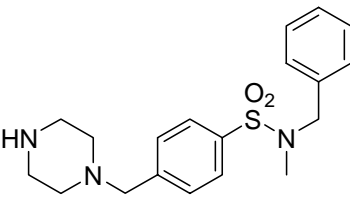
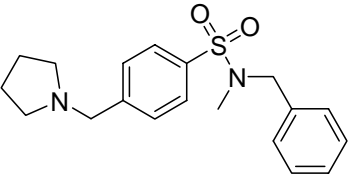
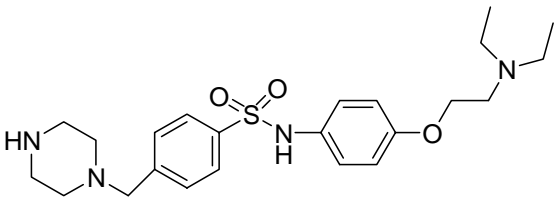
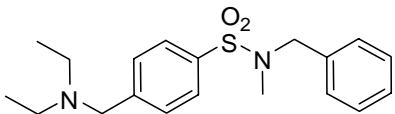
Figure 7.3 (a) Mapping of the SDF-1 N-terminus binding site (yellow circle); residues in yellow are important for SDF-1 binding. (b) Mapping of T140 binding (orange circle); residues in orange are important for T140 binding. (c) Mapping of CVX15 binding (cyan circle); residues in cyan interact with CVX15. (d) Superposition of SDF-1, T140 and CVX15 binding sites.

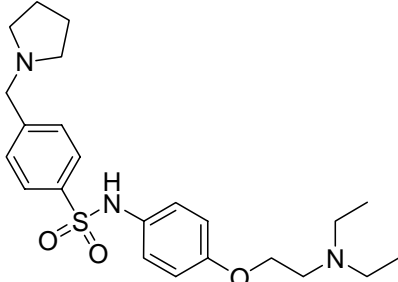
#### 7.2.4 Prediction of Benzene sulfonamide derivatives Binding Poses

Based on the effective concentration (EC), the designed benzene sulfonamides herein can be classified as active or inactive in a competitive binding assay with TN14003. We find that the relative binding free energies of these compounds from Prime MM-GBSA calculations correlate with the effective

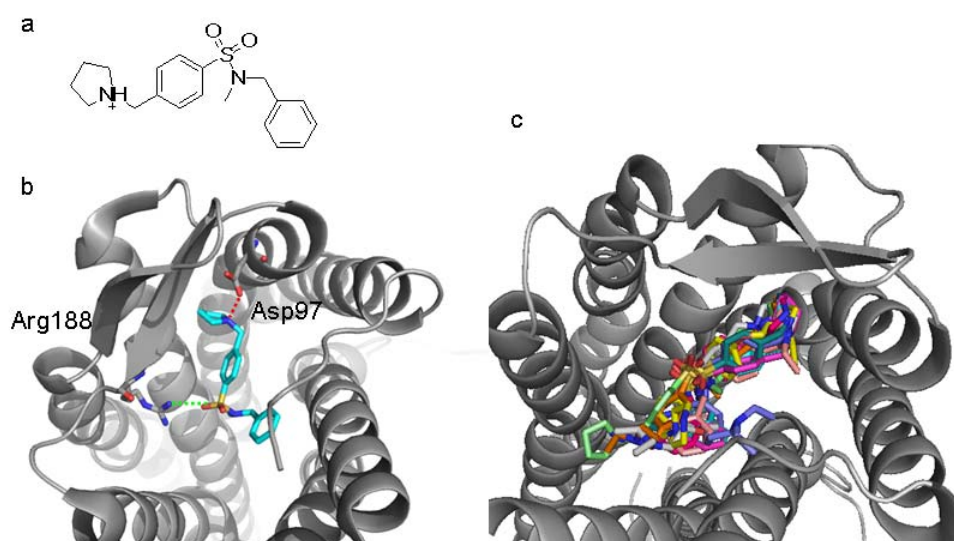
concentrations. For compounds classified as active ( $EC_{50} < 100$  nM), the unscaled binding free energies range from -30 to -40 kcal/mol. (**Table 7.1**) SRM2001 is one of the active compounds with a predicted binding free energy of -36.4 Kcal/mol. The best docking pose of SRM2001 shows that the nitrogen of the pyrrolidine group is protonated and forms a salt bridge (2.8 Å) to Asp97. The oxygen of the sulfonamide group forms hydrogen bond to Arg188. Both pyrrolidine ring and phenyl ring fit into small subpockets and make hydrophobic contacts with CXCR4. (**Figure 7.4b**) Superposition of all active compounds suggests that they bind in a similar location and form either a salt bridge or a hydrogen bond to Asp97 or Glu288, which play key roles in CXCL12 (SDF-1) binding and signal transduction.[110] (**Figure 7.4c**)

Compound	Structure	EC (nM)	MM-GBSA (kcal/mol)
SRM2002		1	-37.4
SRM2016		1	-31.4

<b>SRM2017</b>		1	-29.7
<b>SRM2018</b>		1	-40.3
<b>SRM2019</b>		1	-31.7
<b>SRM2001</b>		10	-36.4
<b>SRM2004</b>		10	-34.5
<b>SRM2008</b>		10	-33.5

SRM2011	 <chem>CCN(CC)CCOC1=CC=C(NS(=O)(=O)C2=CC=C(CN3CCCC3)C2)C1</chem>	10	-34.8
---------	---	----	-------

**Table 7.1:** Effective concentration and unscaled binding free energies for active compounds

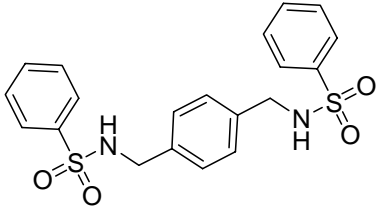
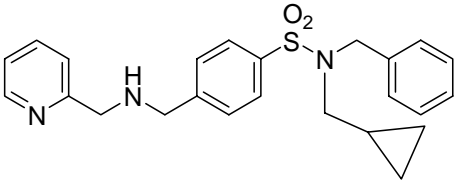
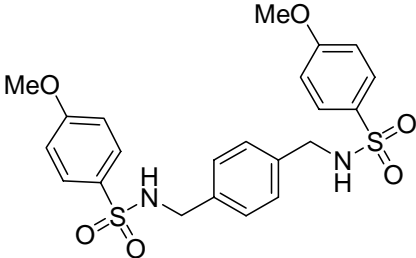


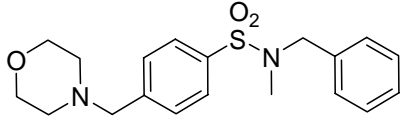
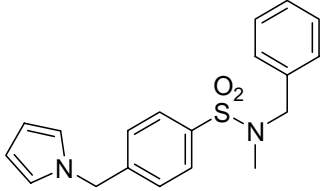
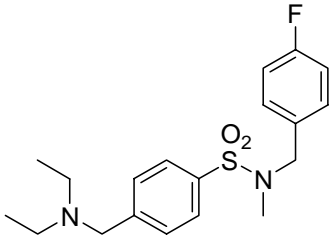
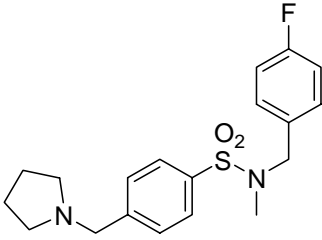
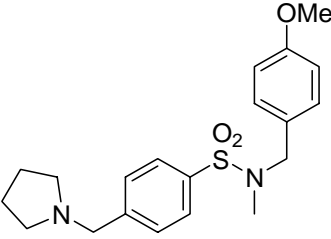
**Figure 7.4:** (a) 2D structure of SRM2011; (b) Best docking pose of SRM2011 in CXCR4; (c) Superposition of all active compound best binding poses in CXCR4.

---

For compounds classified as inactive ( $EC_{50} = 1000$  nM), the relative binding free energies are in the range of -10 to -20 kcal/mol except for SRM2014, SRM2015 and SRM2020. (**Table 7.2**) No polar interactions or hydrogen-bonds are formed between key residues (Asp97, Asp187 or Glu288) in CXCR4 and the first five inactive compounds listed in **Table 7.2**. The best binding pose of SRM2015 shows that this compound occupies part of the pocket which leaves enough space for the simultaneous binding of the cyclic peptide antagonist CVX15. The nitrogen of the pyrrolidine group is protonated and forms a salt bridge (2.7 Å) to Asp97. (**Figure 7.5b**) Superposition of SRM2014, SRM2015 and SRM2020 with predicted binding free energies in the highly active range (-40.0 - -42.1 kcal/mole) illustrates that all of them associate with CXCR4 in similar poses and form salt bridges with Asp97. None show overlap with the CVX15 binding geometry. It is suggested that these three compounds can bind to the CXCR4/CVX15 complex. This explains the inconsistency between the ineffective experimental 1000 nM concentrations and the calculated binding free energies for SRM2014, SRM2015 and SRM2020 reflecting high potency, since TN14003 and CVX15 occupy similar part of the binding pocket. (**Figure 7.5c**) Although these three compounds are inactive in the competitive binding assay with TN14003, they may well be potent compounds for inhibition of SDF-1 binding, since their binding sites overlap with what appears to be the N-terminus of SDF-1 deep in the neck of the receptor (**Figures 7.3a and 7.5c**).

The EC<sub>50</sub> values for some of the analogs are equal to 100 nM, such as SRM2010 and SRM2013. However, the MM-GBSA score for these two showed that SRM2010 are active (MM-GBSA score = -31.4 kcal/mol); and SRM2013 are inactive (MM-GBSA score = -17.7 kcal/mol). Thus, it is necessary to test the IC<sub>50</sub> value for these analogs since this single point EC value is not very accurate. Here, we test the IC<sub>50</sub> values for seven compounds and their MM-GBSA scores and IC<sub>50</sub> values are correlated except SRM2015, which is binding at the SDF-1 N terminus site but not CVX15 site. (**Table 7.3**)

Compound	Structure	EC (nM)	MM-GBSA (kcal/mol)
<b>SRM2000</b>		1000	-21.5
<b>SRM2003</b>		1000	-16.1
<b>SRM2006</b>		1000	-20.7

SRM2007		1000	-13.4
SRM2012		1000	-15.0
SRM2014		1000	-42.1
SRM2015		1000	-40.0
SRM2020		1000	-40.3

**Table 7.2:** Effective concentration and relative binding free energy for inactive compounds

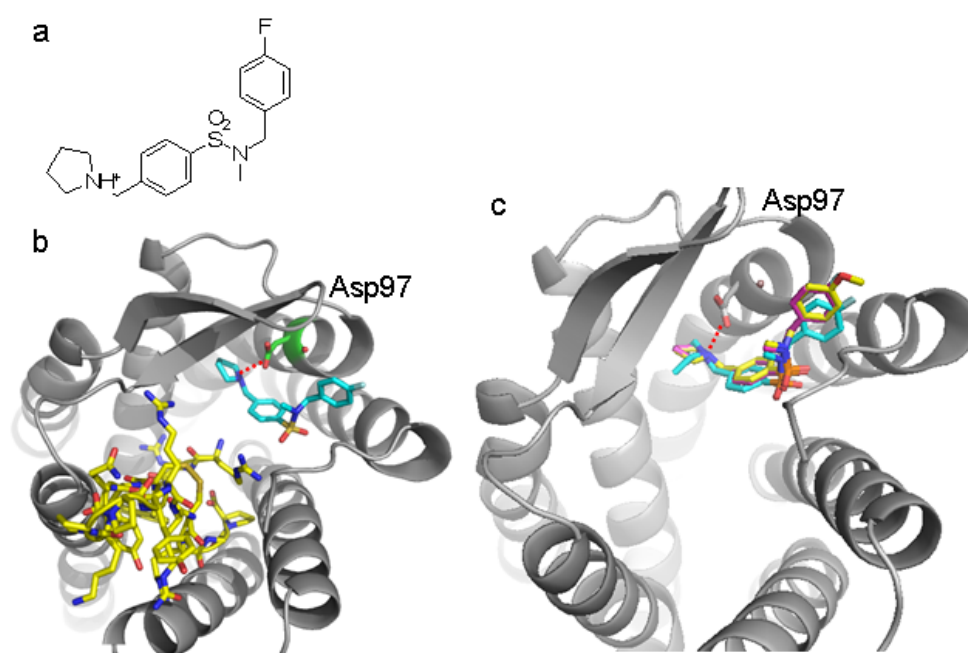


**Figure 7.5:** (a) 2D structure of SRM2015; (b) Best docking pose of SRM2015 (Cyan) in CXCR4 with CVX15 (Yellow); (c) Superposition of best binding poses of SRM2014 (Cyan), SRM2015 (magenta), and SRM2020 (Yellow) in CXCR4.

---

	EC50 (nM)	IC50 (nM)	MMGBSA score (kcal/mol)
SRM2016	1	4.6	-31.4
SRM2001	10	8.0	-36.4
SRM2010	100	21.1	-31.4
SRM2013	100	113	-17.7
SRM2007	1000	5285	-13.4
SRM2012	1000	9849	-15.0
SRM2015	1000	30359	-40.0

**Table 7.3** Effective concentration, IC50 and relative binding free energy for seven compounds

---

## References

1. Madsen, U.K.-L., Povl; Liljefors, Tommy *Madsen, Ulf; Krosgaard-Larsen, Povl; Liljefors, Tommy* (Washington, DC: Taylor & Francis. ISBN 0-415-28288-8, 2002.
2. Tintori, C., F. Manetti, and M. Botta, *Pharmacophoric Models and 3D QSAR Studies of the Adenosine Receptor Ligands*. Current Topics in Medicinal Chemistry, 2010. 10(10): p. 1019-1035.
3. Sali, A., *Meeting on 100,000 protein structures for the biologist* (Avalon, New Jersey, USA). Nature Structural Biology, 1998. 5(12): p. 1029-1032.
4. Prime, V., *Schrodinger, LLC, New York, NY, 2010*.
5. Sammond, D.W., et al., *Computational Design of the Sequence and Structure of a Protein-Binding Peptide*. Journal of the American Chemical Society, 2011. 133(12): p. 4190-4192.
6. Fiser, A., R.K.G. Do, and A. Sali, *Modeling of loops in protein structures*. Protein Science, 2000. 9(9): p. 1753-1773.
7. Zimmer, S.M., et al., *Paclitaxel binding to human and murine MD-2*. Journal of Biological Chemistry, 2008. 283(41): p. 27916-27926.
8. Chang, Y., et al., *Structural basis for G9a-like protein lysine methyltransferase inhibition by BIX-01294*. Nature Structural & Molecular Biology, 2009. 16(3): p. 312-317.
9. Chang, Y., et al., *Adding a Lysine Mimic in the Design of Potent Inhibitors of Histone Lysine Methyltransferases*. Journal of Molecular Biology. 400(1): p. 1-7.
10. Wani, M.C., Taylor, H.L., Wall, M.E., Coggon, P. & McPhail, A.T. Plant antitumor agents, *The isolation and structure of taxol, a novel antileukemic and antitumor agent from Taxus brevifolia*. J Am Chem Soc, 1971. 93,: p. 2325-7.

- 
11. Schiff, P.B., Fant, J. & Horwitz, S.B., *Promotion of microtubule assembly in vitro by taxol*. Nature Biotechnology, 1979. 277: p. 665-7
  12. Horwitz, S.B.e.a., *Taxol: mechanisms of action and resistance*. Ann N Y Acad Sci 1986. 466: p. 733-44.
  13. Snyder, J.P., et al., *The binding conformation of Taxol in beta-tubulin: A model based on electron crystallographic density*. Proceedings of the National Academy of Sciences of the United States of America, 2001. 98(9): p. 5312-5316.
  14. Ganesh, T., et al., *The bioactive Taxol conformation on beta-tubulin: Experimental evidence from highly active constrained analogs*. Proceedings of the National Academy of Sciences of the United States of America, 2004. 101(27): p. 10006-10011.
  15. Ganesh, T., et al., *Evaluation of the tubulin-bound paclitaxel conformation: Synthesis, biology, and SAR studies of C-4 to C-3 ' bridged paclitaxel analogues*. Journal of Medicinal Chemistry, 2007. 50(4): p. 713-725.
  16. Fishman, M.N., et al., *Phase I study of the taxane BMS-188797 in combination with carboplatin administered every 3 weeks in patients with solid malignancies*. Clin Cancer Res, 2006. 12(2): p. 523-8.
  17. Moses, J.W., et al., *Outcomes with the paclitaxel-eluting stent in patients with acute coronary syndromes: analysis from the TAXUS-IV trial*. J Am Coll Cardiol, 2005. 45(8): p. 1165-71.
  18. Kawasaki, K., et al., *Mouse toll-like receptor 4.MD-2 complex mediates lipopolysaccharide-mimetic signal transduction by Taxol*. J Biol Chem, 2000. 275(4): p. 2251-4.
  19. Wang, J., et al., *MyD88 is involved in the signalling pathway for Taxol-induced apoptosis and TNF-alpha expression in human myelomonocytic cells*. Br J Haematol, 2002. 118(2): p. 638-45.
  20. Medzhitov, R., P. Preston-Hurlburt, and C.A. Janeway, Jr., *A human homologue of the Drosophila Toll protein signals activation of adaptive*

- 
- immunity*. Nature, 1997. 388(6640): p. 394-7.
21. Chow, J.C., et al., *Toll-like receptor-4 mediates lipopolysaccharide-induced signal transduction*. J Biol Chem, 1999. 274(16): p. 10689-92.
  22. Ohnishi, T., M. Muroi, and K. Tanamoto, *N-linked glycosylations at Asn(26) and Asn(114) of human MD-2 are required for toll-like receptor 4-mediated activation of NF-kappaB by lipopolysaccharide*. J Immunol, 2001. 167(6): p. 3354-9.
  23. Shimazu, R., et al., *MD-2, a molecule that confers lipopolysaccharide responsiveness on Toll-like receptor 4*. J Exp Med, 1999. 189(11): p. 1777-82.
  24. Ozinsky, A., et al., *The repertoire for pattern recognition of pathogens by the innate immune system is defined by cooperation between toll-like receptors*. Proc Natl Acad Sci U S A, 2000. 97(25): p. 13766-71.
  25. Visintin, A., et al., *Secreted MD-2 is a large polymeric protein that efficiently confers lipopolysaccharide sensitivity to Toll-like receptor 4*. Proc Natl Acad Sci U S A, 2001. 98(21): p. 12156-61.
  26. Nishitani, C., et al., *The Toll-like receptor 4 region Glu(24)-Pro(34) is critical for interaction with MD-2*. Biochem Biophys Res Commun, 2005. 328(2): p. 586-90.
  27. Visintin, A., et al., *Lysines 128 and 132 enable lipopolysaccharide binding to MD-2, leading to Toll-like receptor-4 aggregation and signal transduction*. J Biol Chem, 2003. 278(48): p. 48313-20.
  28. Re, F. and J.L. Strominger, *Separate functional domains of human MD-2 mediate Toll-like receptor 4-binding and lipopolysaccharide responsiveness*. J Immunol, 2003. 171(10): p. 5272-6.
  29. Viriyakosol, S., et al., *MD-2 binds to bacterial lipopolysaccharide*. J Biol Chem, 2001. 276(41): p. 38044-51.
  30. Viriyakosol, S., P.S. Tobias, and T.N. Kirkland, *Mutational analysis of*

- 
- membrane and soluble forms of human MD-2*. J Biol Chem, 2006. 281(17): p. 11955-64.
31. Inohara, N. and G. Nunez, *ML -- a conserved domain involved in innate immunity and lipid metabolism*. Trends Biochem Sci, 2002. 27(5): p. 219-21.
  32. Gruber, A., et al., *Structural model of MD-2 and functional role of its basic amino acid clusters involved in cellular lipopolysaccharide recognition*. J Biol Chem, 2004. 279(27): p. 28475-82.
  33. Derewenda, U., et al., *The crystal structure of a major dust mite allergen Der p 2, and its biological implications*. J Mol Biol, 2002. 318(1): p. 189-97.
  34. Ichikawa, S., et al., *NMR study on the major mite allergen Der f2: Its refined tertiary structure, epitopes for monoclonal antibodies and characteristics shared by ML protein group members*. J Biochem (Tokyo), 2005. 137(3): p. 255-263.
  35. Friedland, N., et al., *Structure of a cholesterol-binding protein deficient in Niemann-Pick type C2 disease*. Proc Natl Acad Sci U S A, 2003. 100(5): p. 2512-7.
  36. Wright, C.S., Q. Zhao, and F. Rastinejad, *Structural analysis of lipid complexes of GM2-activator protein*. J Mol Biol, 2003. 331(4): p. 951-64.
  37. Bertoni, C., et al., *Structural organization and expression of the gene for the mouse GM2 activator protein*. Mamm Genome, 1997. 8(2): p. 90-3.
  38. Ohto, U., et al., *Crystal structures of human MD-2 and its complex with antiendotoxic lipid IVa*. Science, 2007. 316(5831): p. 1632-1634.
  39. Kim, H.M., et al., *Crystal structure of the TLR4-MD-2 complex with bound endotoxin antagonist eritoran*. Cell, 2007. 130(5): p. 906-917.
  40. Kawasaki, K., et al., *Involvement of TLR4/MD-2 complex in species-specific lipopolysaccharide-mimetic signal transduction by Taxol*. J Endotoxin Res, 2001. 7(3): p. 232-6.

- 
41. Kawasaki, K., K. Gomi, and M. Nishijima, *Cutting edge: Gln22 of mouse MD-2 is essential for species-specific lipopolysaccharide mimetic action of taxol*. J Immunol, 2001. 166(1): p. 11-4.
  42. Muroi, M., T. Ohnishi, and K. Tanamoto, *MD-2, a novel accessory molecule, is involved in species-specific actions of Salmonella lipid A*. Infect Immun, 2002. 70(7): p. 3546-50.
  43. Zimmer, S., et al., *Human MD-2 discrimination of meningococcal lipid A structures and activation of TLR4*, in *Glycobiology*. 2007.
  44. Snyder, J.P., et al., *The Conformations of Taxol in Chloroform*. J. Am. Chem. Soc., 2000. 122(4): p. 724-725.
  45. Jayaram, B., D. Sprous, and D.L. Beveridge, *Solvation free energy of biomacromolecules: Parameters for a modified generalized born model consistent with the AMBER force field*. Journal of Physical Chemistry B, 1998. 102(47): p. 9571-9576.
  46. Thompson, J.D., D.G. Higgins, and T.J. Gibson, *CLUSTAL-W - IMPROVING THE SENSITIVITY OF PROGRESSIVE MULTIPLE SEQUENCE ALIGNMENT THROUGH SEQUENCE WEIGHTING, POSITION-SPECIFIC GAP PENALTIES AND WEIGHT MATRIX CHOICE*. Nucleic Acids Research, 1994. 22(22): p. 4673-4680.
  47. Dundas, J., et al., *CASTp: computed atlas of surface topography of proteins with structural and topographical mapping of functionally annotated residues*. Nucleic Acids Research, 2006. 34: p. W116-W118.
  48. Kelly, M.G., et al., *TLR-4 signaling promotes tumor growth and paclitaxel chemoresistance in ovarian cancer*. Cancer Res, 2006. 66(7): p. 3859-68.
  49. Manthey, C.L., et al., *Taxol provides a second signal for murine macrophage tumoricidal activity*. J Immunol, 1994. 152(2): p. 825-31.
  50. Manthey, C.L., et al., *Lipopolysaccharide antagonists block taxol-induced signaling in murine macrophages*. J Exp Med, 1993. 178(2): p. 695-702.
  51. Vogel, S., M.J. Hirschfeld, and P.Y. Perera, *Signal integration in*

- 
- lipopolysaccharide (LPS)-stimulated murine macrophages*. J Endotoxin Res, 2001. 7(3): p. 237-41.
52. Zaks-Zilberman, M., T.Z. Zaks, and S.N. Vogel, *Induction of proinflammatory and chemokine genes by lipopolysaccharide and paclitaxel (Taxol) in murine and human breast cancer cell lines*. Cytokine, 2001. 15(3): p. 156-65.
  53. Manthey, C.L., et al., *Taxol increases steady-state levels of lipopolysaccharide-inducible genes and protein-tyrosine phosphorylation in murine macrophages*. J Immunol, 1992. 149(7): p. 2459-65.
  54. Kawasaki, K., H. Nogawa, and M. Nishijima, *Identification of mouse MD-2 residues important for forming the cell surface TLR4-MD-2 complex recognized by anti-TLR4-MD-2 antibodies, and for conferring LPS and taxol responsiveness on mouse TLR4 by alanine-scanning mutagenesis*. J Immunol, 2003. 170(1): p. 413-20.
  55. Gioannini, T.L., et al., *Isolation of an endotoxin-MD-2 complex that produces Toll-like receptor 4-dependent cell activation at picomolar concentrations*. Proc Natl Acad Sci U S A, 2004. 101(12): p. 4186-91.
  56. Pugin, J., et al., *Soluble MD-2 activity in plasma from patients with severe sepsis and septic shock*. Blood, 2004. 104(13): p. 4071-9.
  57. Zughaier, S.M., et al., *Differential induction of the toll-like receptor 4-MyD88-dependent and -independent signaling pathways by endotoxins*. Infect Immun, 2005. 73(5): p. 2940-50.
  58. Mata-Haro, V., et al., *The vaccine adjuvant monophosphoryl lipid A as a TRIF-biased agonist of TLR4*. Science, 2007. 316(5831): p. 1628-32.
  59. Hung, L.C., et al., *A synthetic analog of alpha-galactosylceramide induces macrophage activation via the TLR4-signaling pathways*. Biochem Pharmacol, 2007.
  60. Okamoto, M., et al., *Involvement of Toll-like receptor 4 signaling in interferon-gamma production and antitumor effect by streptococcal agent*

- 
- OK-432. J Natl Cancer Inst, 2003. 95(4): p. 316-26.
61. Okamoto, M. and M. Sato, *Toll-like receptor signaling in anti-cancer immunity*. J Med Invest, 2003. 50(1-2): p. 9-24.
  62. Beutler, B. and E.T. Rietschel, *Innate immune sensing and its roots: the story of endotoxin*. Nature Reviews Immunology, 2003. 3(2): p. 169-176.
  63. Raetz, C.R.H. and C. Whitfield, *Lipopolysaccharide endotoxins*. Annual Review of Biochemistry, 2002. 71: p. 635-700.
  64. Montminy, S.W., et al., *Virulence factors of Yersinia pestis are overcome by a strong lipopolysaccharide response*. Nature Immunology, 2006. 7(10): p. 1066-1073.
  65. Vincent, J.L., et al., *Clinical expert round table discussion (session 5) at the Margaux Conference on Critical Illness: Outcomes of clinical trials in sepsis: Lessons learned*. Critical Care Medicine, 2001. 29(7): p. S136-S137.
  66. Jack, R.S., et al., *Lipopolysaccharide-binding protein is required to combat a murine Gram-negative bacterial infection*. Nature, 1997. 389(6652): p. 742-745.
  67. Miyake, K., et al. *Essential role of MD-2 in B-cell responses to lipopolysaccharide and Toll-like receptor 4 distribution*. in *7th Biennial Conference of the International-Endotoxin-Society*. 2002. Washington, D.C.
  68. Poltorak, A., et al., *Physical contact between lipopolysaccharide and Toll-like receptor 4 revealed by genetic complementation*. Proceedings of the National Academy of Sciences of the United States of America, 2000. 97(5): p. 2163-2167.
  69. Medzhitov, R., P. PrestonHurlburt, and C.A. Janeway, *A human homologue of the Drosophila Toll protein signals activation of adaptive immunity*. Nature, 1997. 388(6640): p. 394-397.
  70. Viriyakosol, S., et al., *MD-2 binds to bacterial lipopolysaccharide*. Journal

- 
- of Biological Chemistry, 2001. 276(41): p. 38044-38051.
71. Ghose, A.K., V.N. Viswanadhan, and J.J. Wendoloski, *Prediction of hydrophobic (lipophilic) properties of small organic molecules using fragmental methods: An analysis of ALOGP and CLOGP methods*. Journal of Physical Chemistry A, 1998. 102(21): p. 3762-3772.
  72. Gray, J.J., et al., *Protein-protein docking with simultaneous optimization of rigid-body displacement and side-chain conformations*. Journal of Molecular Biology, 2003. 331(1): p. 281-299.
  73. Zimmer SM, L.J., Clayton JL, Stephens DS, Snyder JP., *Paclitaxel Binding to Human and Murine MD-2*. Journal of Biological Chemistry, 2008. 283(41): p. 27916-27926.
  74. Park, B.S., et al., *The structural basis of lipopolysaccharide recognition by the TLR4-MD-2 complex*. Nature, 2009. 458(7242): p. 1191-U130.
  75. Morris, G.M., et al., *Automated docking using a Lamarckian genetic algorithm and an empirical binding free energy function*. Journal of Computational Chemistry, 1998. 19(14): p. 1639-1662.
  76. Park, B.S., et al., *The structural basis of lipopolysaccharide recognition by the TLR4-MD-2 complex*. Nature, 2009. 458(7242): p. 1191-U130.
  77. Krause, N., *Modern Organocopper Chemistry*. Germany, 2002.
  78. Beletskaya, I.P. and A.V. Cheprakov, *Copper in cross-coupling reactions - The post-Ullmann chemistry*. Coordination Chemistry Reviews, 2004. 248(21-24): p. 2337-2364.
  79. Bertz, S.H., et al., *Organocuprate cross-coupling: The central role of the copper(III) intermediate and the importance of the Copper(I) precursor*. Angewandte Chemie-International Edition, 2007. 46(37): p. 7082-7085.
  80. Bertz, S.H., et al., *PREPARATION OF ETHEREAL LITHIUM DIMETHYLCUPRATES (ME(2)CULI)(2) AND ME(2)CULI.LII DISPLAYING NARROW-LINE WIDTH C-13 NMR RESONANCES*. Organometallics, 1995. 14(3): p. 1213-1220.

- 
81. Yamanaka, M., A. Inagaki, and E. Nakamura, *Theoretical studies on structures and reactivities of organocuprate(I) and organocopper(III) species*. Journal of Computational Chemistry, 2003. 24(12): p. 1401-1409.
  82. Jenuwein, T., *The epigenetic magic of histone lysine methylation*. Febs Journal, 2006. 273(14): p. 3121-3135.
  83. Thiery, J.P. and J.P. Sleeman, *Complex networks orchestrate epithelial-mesenchymal transitions*. Nature Reviews Molecular Cell Biology, 2006. 7(2): p. 131-142.
  84. Nishio, H. and M.J. Walsh, *CCAAT displacement protein/cut homolog recruits G9a histone lysine methyltransferase to repress transcription*. Proceedings of the National Academy of Sciences of the United States of America, 2004. 101(31): p. 11257-11262.
  85. Michl, P., et al., *CUTL1 is a target of TGF beta signaling that enhances cancer cell motility and invasiveness*. Cancer Cell, 2005. 7(6): p. 521-532.
  86. Sparmann, A. and M. van Lohuizen, *Polycomb silencers control cell fate, development and cancer*. Nature Reviews Cancer, 2006. 6(11): p. 846-856.
  87. Takeshita, F., et al., *Efficient delivery of small interfering RNA to bone-metastatic tumors by using atelocollagen in vivo*. Proceedings of the National Academy of Sciences of the United States of America, 2005. 102(34): p. 12177-12182.
  88. Hamamoto, R., et al., *SMYD3 encodes a histone methyltransferase involved in the proliferation of cancer cells*. Nature Cell Biology, 2004. 6(8): p. 731-740.
  89. Schneider, R., A.J. Bannister, and T. Kouzarides, *Unsafe SETs: histone lysine methyltransferases and cancer*. Trends in Biochemical Sciences, 2002. 27(8): p. 396-402.
  90. Greiner, D., et al., *Identification of a specific inhibitor of the histone methyltransferase SU(VAR)3-9*. Nature Chemical Biology, 2005. 1(3): p.

- 
- 143-145.
91. Mai, A., et al., *Epigenetic multiple ligands: Mixed Histone/Protein methyltransferase, acetyltransferase, and class III deacetylase (Sirtuin) inhibitors*. Journal of Medicinal Chemistry, 2008. 51(7): p. 2279-2290.
  92. Kubicek, S., et al., *Reversal of H3K9me2 by a small-molecule inhibitor for the G9a histone methyltransferase*. Molecular Cell, 2007. 25(3): p. 473-481.
  93. Takahashi, K. and S. Yamanaka, *Induction of pluripotent stem cells from mouse embryonic and adult fibroblast cultures by defined factors*. Cell, 2006. 126(4): p. 663-676.
  94. Shi, Y., et al., *A combined chemical and genetic approach for the generation of induced pluripotent stem cells*. Cell Stem Cell, 2008. 2(6): p. 525-528.
  95. Chang, Y.Q., et al., *Structural basis for G9a-like protein lysine methyltransferase inhibition by BIX-01294*. Nature Structural & Molecular Biology, 2009. 16(3): p. 312-317.
  96. Muller, A., et al., *Involvement of chemokine receptors in breast cancer metastasis*. Nature, 2001. 410(6824): p. 50-56.
  97. Bajetto, A., et al., *Chemokines and their receptors in the central nervous system*. Frontiers in Neuroendocrinology, 2001. 22(3): p. 147-184.
  98. Zlotnik, A., *Chemokines and cancer*. Int J Cancer, 2006. 119: p. 2026-9.
  99. Fulton, A.M., *Chemokine Receptors in Cancer*. Chemokine Receptors in Cancer, 2009.
  100. Lazennec, G. and A. Richmond, *Chemokines and chemokine receptors: new insights into cancer-related inflammation*. Trends Mol Med, 2010. 16(3): p. 133-44.
  101. Zaitseva, M., et al., *Expression and function of CCR5 and CXCR4 on human Langerhans cells and macrophages: implications for HIV primary infection*. Nat Med, 1997. 3(12): p. 1369-75.

- 
102. Sanchez, X., et al., *Activation of HIV-1 coreceptor (CXCR4) mediates myelosuppression*. J Biol Chem, 1997. 272(44): p. 27529-31.
  103. Feng, Y., et al., *HIV-1 entry cofactor: functional cDNA cloning of a seven-transmembrane, G protein-coupled receptor*. Science, 1996. 272(5263): p. 872-7.
  104. De Clercq, E., *The bicyclam AMD3100 story*. Nat Rev Drug Discov, 2003. 2(7): p. 581-7.
  105. Zhan, W., et al., *Discovery of small molecule CXCR4 antagonists*. J Med Chem, 2007. 50(23): p. 5655-64.
  106. Zhu, A., et al., *Dipyrimidine amines: a novel class of chemokine receptor type 4 antagonists with high specificity*. J Med Chem. 53(24): p. 8556-68.
  107. Liang, Z., et al., *Inhibition of breast cancer metastasis by selective synthetic polypeptide against CXCR4*. Cancer Res, 2004. 64(12): p. 4302-8.
  108. ACD/Labs, Advanced Chemistry Development Inc.
  109. Wu, B., et al., *Structures of the CXCR4 Chemokine GPCR with Small-Molecule and Cyclic Peptide Antagonists*. Science. 330(6007): p. 1066-1071.
  110. Brelot, A., et al., *Identification of residues of CXCR4 critical for human immunodeficiency virus coreceptor and chemokine receptor activities*. Journal of Biological Chemistry, 2000. 275(31): p. 23736-23744.
  111. Choi, W.T., et al., *Unique ligand binding sites on CXCR4 probed by a chemical biology approach: Implications for the design of selective human immunodeficiency virus type 1 inhibitors*. Journal of Virology, 2005. 79(24): p. 15398-15404.
  112. Trent, J.O., et al., *Lipid bilayer simulations of CXCR4 with inverse agonists and weak partial agonists*. Journal of Biological Chemistry, 2003. 278(47): p. 47136-47144.

